J. Fluid Mech. (2014), *vol.* 745, *pp.* 62–91. © Cambridge University Press 2014
doi:10.1017/jfm.2014.96

Stochastic modelling of transverse wave instability in a liquid-propellant rocket engine

Pavel P. Popov, Athanasios Sideris and William A. Sirignano†

Department of Mechanical and Aerospace Engineering, University of California, Irvine, CA 92697, USA

(Received 31 May 2013; revised 11 February 2014; accepted 13 February 2014;
first published online 17 March 2014)

The combustion stability of a liquid-propellant rocket engine experiencing a random, finite perturbation from steady-state conditions is examined. The probability is estimated for a nonlinear resonant limit-cycle oscillation to be triggered by a random disturbance. Transverse pressure waves are considered by using a previously published two-dimensional nonlinear pressure wave equation coupled with Euler equations governing the velocity components. The cylindrical combustion chamber is a complex system containing multiple co-axial methane–oxygen injectors; each co-axial jet is analysed for mixing and burning on its own local grid scheme, with the energy release rate coupled to the wave oscillation on the more global grid. Two types of stochastic forcing for the random disturbance are explored: a travelling Gaussian pressure pulse and an oscillating pressure dipole source. The random variables describing the pulse are magnitude, location, duration and orientation of the disturbances. The polynomial chaos expansion (PCE) method is used to determine the long-time behaviour and infer the asymptote of the solution to the governing partial differential equations. Depending on the random disturbance, the asymptote could be the steady-state solution or a limit-cycle oscillation, e.g. a first tangential travelling wave mode. The asymptotic outcome is cast as a stochastic variable which is determined as a function of input random variables. The accuracy of the PCE application is compared with a Monte Carlo calculation and is shown to be significantly less costly for similar accuracy.

Key words: combustion, computational methods, nonlinear instability

1. Introduction

The problem of liquid-propellant rocket engine (LPRE) combustion instability is a well-known phenomenon in rocket design. The high energy release by combustion can, in certain conditions, reinforce acoustic oscillations which grow to destructive amplitudes. LPRE combustion instability provides a very interesting nonlinear dynamics problem as shown by both theory and experiment (Harrje & Reardon 1972; Oefelein & Yang 1993; Sirignano & Popov 2013).

The combustion chamber, like any partially confined volume filled with gas, has an infinite number of natural acoustic resonant modes. In some operational domains, linear theory predicts that any small disturbance in the noise range can grow to a finite-amplitude limit-cycle acoustic oscillation driven by the combustion process.

† Email address for correspondence: sirignan@uci.edu

https://doi.org/10.1017/jfm.2014.96 Published online by Cambridge University Press

In another type of operational domain, any disturbance, whether in the noise range or substantially larger, will decay in time; the only limit cycle is the steady-state equilibrium. We will focus here on the third type of operational domain, where both an unstable and a stable limit-cycle oscillation exist; that is, noise and larger disturbances up to some threshold level will decay with time. However, above that threshold level, disturbances will develop in time towards the stable limit-cycle oscillation, which has an amplitude higher than the threshold level, i.e. the amplitude of the unstable limit cycle. Disturbances of magnitude greater than the stable limit-cycle amplitude would decay to it but not below it. LPRE oscillations that can result only from disturbances greater than the threshold value have been termed 'triggered combustion instability' in the literature. A disruption in propellant mass flow or a very large fluctuation caused by transient operation can provide the necessary trigger. Triggered instability presents the greater challenge and is emphasized here.

In this paper we focus on the bi-stable operating domain of the engine, where triggering is possible and both an unstable limit cycle and a greater-amplitude stable limit cycle exist. Neighbouring operating domains with different parameters, e.g. mean pressure, mass flow and mixture ratio, can be unconditionally stable (i.e. have no limit-cycle oscillation) or unconditionally unstable (i.e. have a stable limit-cycle oscillation). The operation parameters remain constant with time; consequently, drift will not occur from one domain to another during engine operation.

Our approach differs from previous research in that we consider triggering disturbances as random events. In § 1.1, we discuss briefly the previous literature on LPRE combustion instability and give a description of the phenomenon. In § 1.2, we discuss in more detail the uncertainties associated with triggering and review the literature on polynomial chaos expansions, the main tool used in the stochastic analysis presented here.

1.1. *Review of LPRE combustion instability literature*

The history of theoretical and computational research on LPRE combustion instability will be briefly reviewed, followed by an explanation of the new methods and goals of this current research.

The leading work during the 1950s and 1960s on linear and nonlinear theoretical descriptions of LPRE wave dynamics was due to Professor Luigi Crocco and his students. Linear instability was addressed extensively by Crocco & Cheng (1953, 1956) and Reardon, Crocco & Harrje (1964). The heuristic, two-parameter (n, τ) coupling between combustion and acoustics was developed, along with the first method for superposition of two continua for two phases (condensed phase and gas) for any application. The early work of Tsien (1952) on acoustical reflections in the nozzle and handling of the throat singularity was extended to address three-dimensional linear oscillations in rocket engines (Reardon *et al.* 1964; Crocco & Sirignano 1967). Further nonlinear perturbation studies by Sirignano (1964), Sirignano & Crocco (1964), Zinn (1968), Crocco & Mitchell (1969) and Mitchell, Crocco & Sirignano (1969) showed the existence of both unstable and stable limit-cycle oscillations for the longitudinal mode, sometimes with shock wave formation, and for the transverse modes. The unstable limit cycle provides a threshold for triggering: below this amplitude, disturbances decay in time to zero amplitude, whereas above it, growth to larger amplitude occurs. The approach predicts either a stable or an unstable limit cycle for each point in the (n, τ) plane near the linear stability limit line.

Zinn & Powell (1971) introduced the Galerkin method to the field, still using (n, τ) methods. Culick and coworkers used an eigenfunction expansion together with

https://doi.org/10.1017/jfm.2014.96 Published online by Cambridge University Press

a two-time variable technique that had some of the same advantages (see Awad & Culick 1986; Yang, Kim & Culick 1990; Culick 1994, 2006). More recently, a Galerkin approach (also known as reduced-basis modelling) has been employed by Flandro, Fischbach & Majdalani (2007) and Jacob *et al.* (2010).

Over several decades, some progress has been made in understanding the mechanisms driving the LPRE instability for thermodynamic subcritical and transcritical operations where vaporization is rate-controlling (Priem & Heidmann 1960; Heidmann & Wieber 1965; Strahle 1965*a*,*b*,*c*, 1967; Tong & Sirignano 1989; Bhatia & Sirignano 1991; Delplanque & Sirignano 1993; Yang & Lin 1994; Sirignano *et al.* 1995; Delplanque & Sirignano 1996; Duvvur, Chiang & Sirignano 1996; Sirignano 2010).

Interest in propellant combinations of hydrocarbon fuel and oxygen, stored as liquids, is returning to the LPRE field. The analysis and results here will address situations where the methane and oxygen propellants are injected co-axially as gases. These propellants will have elevated temperatures at the injectors because they have been used prior to injection as a coolant.

Numerical simulations can be used to probe and understand the rocket motor as a complex system and to predict instability. At this time, large-eddy simulations exist for simple configurations. There are several single injector studies (Oefelein & Yang 1998; Oefelein 2006; Tucker *et al.* 2007; Yang, Cuoco & Oschwald 2007; Tucker *et al.* 2008; Masquelet *et al.* 2009; Masquelet & Menon 2010; Schmitt *et al.* 2010, 2011; Guézennec, Masquelet & Menon 2012), but systematic large-eddy simulation of a multi-injector system is still to be demonstrated.

1.2. *Uncertainty of triggering disturbances*

The disturbances that trigger combustion instability can result from fluid-mechanical disruptions in the propellant injection process, shedding of large rogue vortices through the choked nozzle, extraordinary excursions in local burning rates or a synergism amongst such events. The disturbances cause a perturbation in local pressure and velocity for some duration and may be sufficient to trigger a resonant oscillation in the combustion chamber. Disturbances can be described by their magnitude, spatial orientation, location, beginning time and duration. Typically, the rocket engineer does not know these characteristics *a priori*; therefore, these parameters bear uncertainty and may be described as stochastic variables. Thus, this nonlinear dynamics problem may properly be viewed as stochastic. Although the eventual limit cycle can be described in a deterministic manner, there is uncertainty about the trigger that provides the path to the limit cycle. There are advantages in applying a stochastic analysis to this problem. To this end, the deterministic simulations of Sirignano & Popov (2013) are extended to a more general problem, in which the perturbation from the steady-state operational conditions, and therefore the entire solution, is a random variable. This allows for modelling of the uncertainty about key features of the perturbation, such as its location, duration, orientation and amplitude. The model can be useful for minimizing the probability of instability.

The stochastic nature of the combustion pertains especially to the initiation mechanism which moves the dynamics from the steady state (or non-oscillatory starting transient) to a stable limit cycle (the periodic or chaotic nonlinear oscillation). The limit cycles and the equilibrium points are deterministic, but the path to them can be stochastic.

Thus, to understand the source and the result of perturbation with the consequent instability mechanism, the rocket engine, with its very large number of propellant

https://doi.org/10.1017/jfm.2014.96 Published online by Cambridge University Press

injector streams, can be viewed as a complex system. Each of these streams is a component with semi-autonomy but strong coupling with other streams and with the overall chamber wave dynamics. Complex systems are characterized by: (*a*) many semi-autonomous components or subsystems; (*b*) connectivity (networking) amongst the complex-system components; (*c*) a multiscale structure; (*d*) a self-organizing capability such that the overall structure and macro-level behaviour can emerge from the interactions amongst the components (nonlinear synergism amongst the components is vital); and (*e*) unpredictable behaviour, including chaotic behaviour (Bar-Yam 1996; Ottino 2004). Therefore, the characteristics of a complex system can be seen in the reacting flow of a liquid-propellant rocket engine, and a stochastic approach to describing the instability mechanism relating a perturbation with its long-time consequence can potentially lead to significant insights.

In order to obtain an accurate solution to this stochastic problem in an efficient computational manner, we employ a polynomial chaos expansion (PCE) (Xiu & Karniadakis 2002; Xiu 2010) that expresses the solution as a truncated series of polynomials in the random variables (RVs). PCEs in terms of Hermite polynomials of Gaussian RVs were introduced by Wiener (1938), and their convergence properties were studied by Cameron & Martin (1947). Spectral methods for uncertainty quantification have been used to study the phenomenon of turbulence (Meecham & Jeng 1968; Chorin 1970). PCEs were first used in an engineering context by Ghanem & Spanos (1990) for solving stochastic structural dynamics problems. In Xiu & Karniadakis (2002), generalized polynomial chaos is introduced via the Wiener–Askey scheme by matching the family of orthogonal polynomials used to the probability density function (PDF) of the RVs to ensure optimal convergence. Since then, PCE methods have been effectively applied in many different engineering fields, including fluid flow (Le Maître *et al.* 2001, 2002; Xiu & Karniadakis 2003; Lin, Su & Karniadakis 2006), heat transfer (Hien & Kleiber 1997; Sluzalec 2000; Liu, Hu & Yu 2001), flow–structure interaction (Xiu *et al.* 2002; Witteveen, Sarkar & Bijl 2007), computational fluid dynamics (Knio & Le Maître 2006) and reacting-flow systems (Phenix *et al.* 1998; Reagan *et al.* 2003; Mendes, Pereira & Pereira 2011).

Although PCE has been used before to study nonlinear oscillations in lumped dynamical systems, to the best of the authors' knowledge it has not been applied for this purpose in distributed parameter systems and, in particular, not for the study of triggered oscillations in a combustion process. Nonlinear oscillations present a challenging application of PCE methods, as these methods have difficulty approximating the long-term solutions of dynamical equations; indeed, convergence of the PCE is not uniform with respect to the time variable. In Beran, Pettit & Millman (2006) and Witteveen *et al.* (2008), the problem of flutter in aeroelastic systems manifesting as limit-cycle oscillations is studied with PCE methods, and the long-term time integration issue is considered. More specifically, Beran *et al.* (2006) used the Wiener–Haar expansion with basis functions having local support instead of the more traditional PCE global basis functions, and were able to demonstrate improved behaviour; Witteveen *et al.* (2008) employed a probabilistic collocation method to approximate time-independent variables of the RVs that in turn are used to approximate a cycle of the oscillation. In this paper, we deal with this issue by simply selecting a fixed time window so that enough cycles of the oscillation are included to enable one to infer properly the existence or non-existence of a triggered instability. With enough terms in the PCE, the solution within this time window can be accurately represented. As will be discussed later in detail, it is possible to capture the triggering of unstable oscillations with a modest number of terms in the PCE, at a computational cost considerably smaller than that of a more traditional Monte Carlo approach.

https://doi.org/10.1017/jfm.2014.96 Published online by Cambridge University Press

The remainder of this paper is organized as follows. In § 2 the governing equations for the wave dynamics and the jet mixing and reaction are introduced, and the PCE approximation to the stochastic solution is described. Section 3 provides the details of the numerical solution as well as analytical expressions for the stochastic disturbances to the flow that can possibly trigger the large-amplitude transverse acoustic oscillation. Results are reported in § 4: findings are presented concerning the long-time behaviour of the primitive variables such as pressure and the ability to predict limit-cycle oscillations from a finite time window; also, error estimates and validation for the PCE method are given. We identify those pulse characteristics that are more likely to cause growth of a limit-cycle pressure wave and study the dependencies of the triggering probability upon the various characteristics of the perturbing pulses. Finally, the computational cost versus accuracy of the PCE method in comparison with a Monte Carlo method is discussed. The major conclusions are drawn in § 5.

2. Governing equations

Transverse spinning acoustic waves can grow to higher amplitudes than do axial waves (Harrje & Reardon 1972). This may be attributed to the presence in the latter of dissipative shock waves, which are absent in transverse spinning waves. We therefore focus on transverse waves because they are more destructive in general. A simplified two-dimensional model will be used; it was introduced by Sirignano & Popov (2013) and applied to a deterministic set of disturbances that have been found to trigger instabilities when their magnitude is sufficiently large.

The cylindrical combustion chamber will have the injector face at one end and the choked nozzle at the other end. Many co-axial injector ports will be present to supply the two propellant flows with oxygen flowing from the inner duct and methane flowing through the surrounding annulus. Pressure is sufficiently high and there is sufficient preheating of the propellants to consider propellants and products as compressible fluids. The deviation from steady-state operation will be governed by a system of equations involving the nonlinear wave equation for chamber pressure coupled with Euler equations for the velocity components (Sirignano & Popov 2013). A multiscale approach will be followed where effects of viscosity, turbulence and thermal and mass diffusion are neglected on the scale of the oscillation wavelength or chamber diameter but are considered in the jet flame region surrounding the exit flow from each injector.

First, we describe the governing equations for a deterministic system with known initial conditions. Then, we shall present the polynomial chaos expansion method which converts this deterministic system into a system of stochastic partial differential equations.

2.1. *Deterministic simulation of transverse wave instability*

Here we summarize the governing two-dimensional deterministic model equations for a transverse wave instability simulation. A more detailed description of the derivation of these equations can be found in Sirignano & Popov (2013). Similarly to that work, we assume that the propellants in the chamber are at supercritical pressure and hence can be modelled as a single-phase gas. For simplicity, perfect gas behaviour, with a constant specific heat ratio, is assumed. Following a standard practice in LPRE instability analysis, we neglect those wavy variations in the scalar fields (e.g. entropy or temperature) which result from kinematic waves moving primarily in the main flow

https://doi.org/10.1017/jfm.2014.96 Published online by Cambridge University Press

direction (i.e. the x direction) and whose length scales are small compared with the acoustic wavelength and the chamber diameter. Such short wavelengths are expected to be diffused quickly in the turbulent combustion chamber environment.

The perfect gas law is used, although a cubic equation of state would generally be superior. Qualitatively, the same behaviour as a perfect gas would occur at high pressure and temperature: pressure would increase with temperature at constant density and increase with density at constant temperature. For the cases we study, the quantitative error is quite small and the perfect gas approximation is acceptable. As an example, for the carbon dioxide product at the representative conditions of 200 atm and 2000 K, the classical van der Waals equation of state corrects the density predicted by the perfect gas law by less than 3 %. For water vapour, the same correction is less than 1 %. (The more accurate Redlich–Kwong equation of state is known to give values that lie between those of van der Waals and the perfect gas law, thereby predicting lower error.) The compression of the gas at constant temperature would increase substantially the effect of the molecular interactions. However, at the high temperatures of interest, the expansive tendency due to temperature balances somewhat the compression due to increased pressure, moderating the molecular interaction and the need for correction in the equation of state.

The inviscid forms of the continuity, momentum and energy equations were used to develop a three-dimensional nonlinear wave equation. Wavelengths are sufficiently long to justify the neglect of viscous and diffusion terms in the development of this wave equation. The analysis focuses on pure tangential modes of oscillation without longitudinal-mode coupling. Therefore, the pressure variation in the primary flow direction, i.e. over the x variable, is very slight compared to variations in the transverse plane. The three-dimensional wave equation, azimuthal momentum equation and radial momentum equations are integrated over the x variable, from injector face to nozzle entrance. The differences between the averages of products (or squares) and the products of two averages (or squares of an average) were neglected.

The wave equation for pressure is averaged in the axial x direction to yield the following two-dimensional evolution equation for the longitudinal average of pressure:

$$\begin{aligned}
&\frac{\partial^2 p}{\partial t^2} + Ap^{(\gamma-1)/(2\gamma)}\frac{\partial p}{\partial t} - Bp^{(\gamma-1)/\gamma}\left[\frac{\partial^2 p}{\partial r^2} + \frac{1}{r}\frac{\partial p}{\partial r} + \frac{1}{r^2}\frac{\partial^2 p}{\partial \theta^2}\right] \\
&\quad = \frac{(\gamma-1)}{\gamma}\frac{1}{p}\left(\frac{\partial p}{\partial t}\right)^2 + (\gamma-1)\frac{\partial E}{\partial t} + \gamma p^{(\gamma-1)/\gamma}\left[\frac{\partial^2\left(p^{1/\gamma}u_r^2\right)}{\partial r^2} + \frac{2}{r}\frac{\partial\left(p^{1/\gamma}u_r^2\right)}{\partial r}\right. \\
&\qquad \left. + \frac{2}{r}\frac{\partial^2\left(p^{1/\gamma}u_r u_\theta\right)}{\partial r\partial\theta} + \frac{2}{r^2}\frac{\partial\left(p^{1/\gamma}u_r u_\theta\right)}{\partial\theta} + \frac{1}{r^2}\frac{\partial^2\left(p^{1/\gamma}u_\theta^2\right)}{\partial\theta^2} - \frac{1}{r}\frac{\partial\left(p^{1/\gamma}u_\theta^2\right)}{\partial r}\right] \qquad (2.1)
\end{aligned}$$

where r and θ are the radial and azimuthal coordinates, p denotes pressure, u denotes velocity, and γ is the specific heat ratio. Here E is the energy release rate, and A and B are constants that depend on the steady-state temperature and pressure, as well as on the ratio between the throat and entrance areas of the nozzle:

$$B = \frac{a_0^2}{p_0^{(\gamma-1)/\gamma}}, \qquad (2.2)$$

$$A = \frac{KB}{L} \qquad (2.3)$$

https://doi.org/10.1017/jfm.2014.96 Published online by Cambridge University Press

where

$$K = \frac{\gamma+1}{2\gamma}\frac{A_{throat}}{A_{entrance}}\left(\frac{\gamma}{R_m}\right)^{1/2}\left(\frac{\gamma+1}{2}\right)^{-(\gamma+1)/(2(\gamma-1))}\frac{p_0^{(\gamma-1)/(2\gamma)}}{T_0^{1/2}}, \tag{2.4}$$

with p_0, T_0 and a_0 denoting, respectively, the pressure, temperature and speed of sound of the undisturbed chamber, and A_{throat} and $A_{entrance}$ the throat and entrance areas of the nozzle. Here L is chamber length and R_m is the specific gas constant.

The integration of the x-derivatives yielded terms at the injector plane and nozzle-entrance plane where boundary conditions were applied. The nozzle boundary condition of Crocco & Sirignano (1966) was applied. With a short (compared with the wavelength) multi-orifice nozzle, the Mach number at the nozzle entrance remains fixed while the primitive variables oscillate. The mass flow rate at the injector ports is constant during chamber oscillation. Consequently, this integration left conditions at the nozzle-entrance plane in the two-dimensional wave equation. Specifically, the resulting term is the first-derivative-with-respect-to-time term on the left-hand side of (2.1). The nozzle will have a damping effect on the oscillation, depending on the details of the design and the particular oscillation character.

The two momentum equations are averaged in the axial direction to yield

$$\frac{\partial u_r}{\partial t} + u_r\frac{\partial u_r}{\partial r} + u_\theta\frac{1}{r}\frac{\partial u_r}{\partial \theta} - \frac{u_\theta^2}{r} + \frac{C}{p^{1/\gamma}}\frac{\partial p}{\partial r} = 0, \tag{2.5}$$

$$\frac{\partial u_\theta}{\partial t} + u_r\frac{\partial u_\theta}{\partial r} + u_\theta\frac{1}{r}\frac{\partial u_\theta}{\partial \theta} + \frac{u_r u_\theta}{r} + \frac{C}{rp^{1/\gamma}}\frac{\partial p}{\partial \theta} = 0, \tag{2.6}$$

with $C = p_0^{1/\gamma}/\rho_0$.

The co-axial jet mixing and burning for each injector element is analysed with a locally axisymmetric coordinate scheme. The scale of each injector is small enough compared with the acoustic wavelength that transverse pressure variation across the jet may be neglected. Each jet is sufficiently far from its neighbouring jet so that direct interaction is negligible. Each jet couples in a two-way manner with the acoustic field. The coupling of the wave dynamics with the jet mixing and burning occurs through the E term in (2.1).

To obtain the energy release rate E, we introduce the Shvab–Zel'dovich variable $\alpha = Y_F - \nu Y_O$, where Y_F and Y_O are the fuel and oxidizer mass fractions, respectively, and ν is the fuel-to-oxygen mass stoichiometric ratio. The variable $\beta = (Q/(c_p T_o))Y_F - T/T_o + (p/p_o)^{(\gamma-1)/\gamma}$ is introduced. After a boundary-layer approximation to neglect diffusion in the flow direction and an Oseen approximation to allow use of a uniform velocity for the coefficients of the advective and convective terms, we obtain the following set of scalar transport equations:

$$\frac{\partial \alpha}{\partial t} + U(t)\frac{\partial \alpha}{\partial x} - D\left[\frac{\partial^2 \alpha}{\partial \eta^2} + \frac{1}{\eta}\frac{\partial \alpha}{\partial \eta}\right] = 0, \tag{2.7}$$

$$\frac{\partial \beta}{\partial t} + U(t)\frac{\partial \beta}{\partial x} - D\left[\frac{\partial^2 \beta}{\partial \eta^2} + \frac{1}{\eta}\frac{\partial \beta}{\partial \eta}\right] = 0 \tag{2.8}$$

and

$$\frac{\partial Y_F}{\partial t} + U(t)\frac{\partial Y_F}{\partial x} - D\left[\frac{\partial^2 Y_F}{\partial \eta^2} + \frac{1}{\eta}\frac{\partial Y_F}{\partial \eta}\right] = \omega_F. \tag{2.9}$$

https://doi.org/10.1017/jfm.2014.96 Published online by Cambridge University Press

In the above equations, x and η are, respectively, the axial and radial coordinates of one of several axisymmetric cylindrical grids co-axial with each injector, and the source term on the right-hand side of (2.9), after a one-step irreversible Arrhenius chemical mechanism, has the form

$$\begin{aligned}\omega_F &= A_c \rho Y_O Y_F \, \mathrm{e}^{-\epsilon/R_u T} \\ &= \frac{A_c p_o}{\nu R_m T_o} \frac{p}{p_o} \frac{Y_F[Y_F - \alpha]}{(Q/c_p T_o) Y_F - \beta + (p/p_o)^{(\gamma-1)/\gamma}} \\ &\quad \times \exp\left[\frac{\epsilon/R_u T_o}{(Q/c_p T_o) Y_F - \beta + (p/p_o)^{(\gamma-1)/\gamma}}\right], \end{aligned} \tag{2.10}$$

where A_c is the chemical rate constant, ϵ is the activation energy, R_m and R_u are the mixture-specific and universal gas constants, respectively, and the diffusivity D is evaluated based on the turbulent viscosity approximation for a self-similar jet (Pope 2000) with a turbulent Prandtl number of 0.7, yielding

$$D = \frac{U(t) R_o}{24.5}, \tag{2.11}$$

with $U(t)$ being the jet axial velocity. For further details on the derivation of these scalar evolution equations, see Sirignano & Popov (2013). The set of equations (2.7)–(2.11) is applied independently for each jet exiting an injector. Through the pressure effect in (2.10), they couple to the wave dynamics described in (2.1), (2.5) and (2.6). The radial coordinate, η, in (2.7)–(2.9) is the local radial coordinate for each jet and therefore differs from the chamber radial coordinate, r, used in (2.1), (2.5) and (2.6). The integration over the x direction of the result at each time for the reaction rate determined in (2.10) gives the value of E to be substituted into (2.1).

The problem has several similarity parameters that result if the equations were to be non-dimensionalized using the chamber radius and the speed of sound at mean chamber conditions as the reference length and velocity values. Other steady-state conditions would also be used as reference values in the non-dimensional form of the equation. The Mach number at the nozzle-entrance plane is critical; since the multi-orifice short-nozzle configuration makes this value uniform over that plane, it is a similarity parameter fixed by the nozzle design only. The ratio of chamber radius to mean speed of sound, natural period of oscillation, characteristic jet mixing time based on jet diameter and characteristic chemical time are four important time scales and form three relevant time ratios. However, since the mode of oscillation is not known *a priori*, the period of oscillation is not known until a calculation is made. So the most interesting similarity parameters can only be given after the calculation, e.g. the product of the oscillation frequency and the characteristic chemical time or the product of the frequency and mixing time. For this reason, the dimensional form of the equations is used in the calculations.

2.2. *Galerkin approximation of a stochastic PDE system with uncertainty in the initial conditions*

In order to explore more efficiently the behaviour of the combustion chamber, we shall generalize the deterministic problem of the previous subsection by introducing a random initial condition, reflecting the uncertainty in the nature of the disturbance which causes an instability.

Pulses are applied to simulate triggering mechanisms. In order to trigger transverse travelling or spinning waves, an orientation must be associated with the pulse. A

https://doi.org/10.1017/jfm.2014.96 Published online by Cambridge University Press

symmetric pulse such as a solitary monopole can yield only standing waves. Two types of pulses with an orientation are used: (i) two consecutive Gaussian pulses separated very slightly in the initiation time and in the locations of the Gaussian centres; and (ii) a dipole pulse which inherently has an orientation. The first type results in some mass addition, since the superposition of the pulse modifies the density profile and the integral of the density over the volume from the steady-state profile and integral value. It is therefore similar to the gunpowder bombs used in experimental testing and rating of LPREs discussed by Harrje & Reardon (1972). It might also represent a disruption in the rate at which propellants are supplied to the chamber. This type of pulse is called a travelling Gaussian pulse and was introduced by Sirignano & Popov (2013). In this study, we extend that first pulsing approach to examine a pair of travelling pulses with stochastic variables determining the relative timing and relative orientation of each member of the pair. The second type involves negligible mass addition and thereby better represents a natural disruption with the flow and combustion processes in the combustion chamber. Essentially, in this dipole type, a pair of closely adjacent oscillating (but out of phase) monopoles provide an orientation through the relative position of the monopole components and a characteristic time through the oscillation frequency. The general results are qualitatively similar terms of triggering action.

The perturbation from steady-state operating conditions is uniquely determined by a vector, $\boldsymbol{\xi}$, of independent random variables; $\boldsymbol{\xi}$ may either affect the initial condition of (2.1) or determine a forcing function on the right-hand side of (2.1) for a short interval of time at the beginning of the simulation.

Then, the solution of the system of PDEs from the previous subsection, consisting of the fields p, u_i, α, β and Y_F, may be expressed as a set of fields, in the form $[p, u_i] = \boldsymbol{n}(r, \theta, t, \boldsymbol{\xi})$ and $[\alpha^{(j)}, \beta^{(j)}, Y_F^{(j)}] = \boldsymbol{m}(x, \eta, t, \boldsymbol{\xi})$, with the superscript (j) denoting a particular injector from the set of injectors for the given engine design; therefore, the system consisting of (2.1) and (2.5)–(2.9) forms two multivariate PDE systems

$$\mathscr{L}_1(\boldsymbol{n}, r, \theta, t, \boldsymbol{\xi}) = \boldsymbol{f}_1(r, \theta, t, \boldsymbol{m}, \boldsymbol{\xi}), \tag{2.12}$$

$$\mathscr{L}_2(\boldsymbol{m}, x, \eta, t, \boldsymbol{\xi}) = \boldsymbol{f}_2(x, \eta, t, \boldsymbol{n}, \boldsymbol{\xi}), \tag{2.13}$$

where (2.12) governs the evolution of p, u_r and u_θ on a two-dimensional r–θ grid. Equation (2.13) governs the evolution of a certain number of sets (one for each injector) for the fields α, β and Y_F on two-dimensional x–η grids, co-axial with the injector axes. Here $\mathscr{L}_1$ is the differential operator representing (2.1), (2.5) and (2.6), and $\mathscr{L}_2$ is the differential operator representing (2.7)–(2.9); $\boldsymbol{f}_1$ and $\boldsymbol{f}_2$ are source terms. Note that (2.12) and (2.13) are coupled via the dependence on $\boldsymbol{m}$ of $\boldsymbol{f}_1$, the source term in the evolution equation of $\boldsymbol{n}$ (due to the pressure being dependent on the energy release) and, conversely, via the dependence on $\boldsymbol{n}$ of $\boldsymbol{f}_2$ (due to the Y_F source term being dependent on pressure). We shall employ the stochastic Galerkin method to approximate the solutions of (2.12) and (2.13). For an in-depth introduction to the stochastic Galerkin technique, the reader is referred to Xiu (2010).

A truncated polynomial chaos expansion (PCE) consists of the approximations

$$\boldsymbol{n}(r, \theta, t, \boldsymbol{\xi}) \approx \sum_{k=0}^{P} \boldsymbol{n}_k(r, \theta, t)\Psi_k(\boldsymbol{\xi}) \tag{2.14}$$

$$\boldsymbol{m}(x, \eta, t, \boldsymbol{\xi}) \approx \sum_{k=0}^{P} \boldsymbol{m}_k(x, \eta, t)\Psi_k(\boldsymbol{\xi}), \tag{2.15}$$

https://doi.org/10.1017/jfm.2014.96 Published online by Cambridge University Press

where the $\Psi_k(\boldsymbol{\xi})$ are $P+1$ polynomials in the random vector $\boldsymbol{\xi}$. The polynomials Ψ_k are orthogonal with respect to the distribution of ξ and form a set of basis functions. Therefore, the approximations in (2.14) and (2.15) converge in an L_2 sense. In particular, for the present application, which uses uniform random variables, the $\Psi_k(\boldsymbol{\xi})$ for the lth-order PCE expansion are all of the possible n-dimensional products of the Legendre polynomials in the scalar components of $\boldsymbol{\xi}$ of degree up to l. The number of all such polynomials, $P+1$, is equal to $(n+l)!/(n!\,l!)$. For a fixed simulation end time T_F, this representation of the sample space implies spectral convergence of the PCE with respect to the order l (Xiu 2010). This means that the approximation error is $O(l^{-p})$, where p is the highest-order derivative of the solution with respect to $\boldsymbol{\xi}$ that is bounded in L_2. Thus, if the solution is analytic in $\boldsymbol{\xi}$, the convergence rate is exponential. As will be further elaborated in § 4, for the low-dimensional sample space used in this study, the PCE method has substantially better computational efficiency than a standard Monte Carlo procedure.

Substituting the approximations (2.14) and (2.15) into (2.12) and (2.13), and then taking the inner product, denoted by $\langle \cdot \mid \cdot \rangle$, over the range of $\boldsymbol{\xi}$ with each of the polynomials $\Psi_k(\boldsymbol{\xi})$ yields

$$\left\langle \mathscr{L}_1\left(r,\theta,t,\boldsymbol{\xi};\sum_{k=0}^{P}\boldsymbol{n}_k(r,\theta,t)\Psi_k(\boldsymbol{\xi})\right)\,\middle|\,\Psi_i(\boldsymbol{\xi})\right\rangle = \left\langle \boldsymbol{f}_1(r,\theta,t,\boldsymbol{m},\boldsymbol{\xi})\mid\Psi_i(\boldsymbol{\xi})\right\rangle, \quad (2.16)$$

$$\left\langle \mathscr{L}_2\left(x,\eta,t,\boldsymbol{\xi};\sum_{k=0}^{P}\boldsymbol{m}_k(x,\eta,t)\Psi_k(\boldsymbol{\xi})\right)\,\middle|\,\Psi_i(\boldsymbol{\xi})\right\rangle = \left\langle \boldsymbol{f}_2(x,\eta,t,\boldsymbol{n},\boldsymbol{\xi})\mid\Psi_i(\boldsymbol{\xi})\right\rangle, \quad (2.17)$$

which are two systems of $P+1$ deterministic equations, each similar to the system (2.1)–(2.9). They can be solved numerically for each of the $P+1$ coefficients $\boldsymbol{n}_k(r,\theta,t)$ and $\boldsymbol{m}_k(x,\eta,t)$, using the same discretization schemes as for the approximation of a deterministic solution to (2.1)–(2.9).

A sparse grid based on Smolyak's quadrature rule is used to deal with the integration of the nonlinear terms when evaluating the inner products in (2.16) and (2.17). Specifically, we use $Q_i^{(1)}f$ to denote the ith order of a univariate nested quadrature rule (Petras 2003), i.e.

$$Q_i^{(1)}f = \sum_j q_j f(x_j), \quad (2.18)$$

where q_j and x_j are the weights and nodes, respectively, of the ith-order univariate quadrature, with $Q_0^{(1)}f$ being identically zero. We also use $Q^{(d_1)}\times Q^{(d_2)}g$ to denote the product of the multivariate quadratures $Q^{(d_1)}$ and $Q^{(d_2)}$, the first of which integrates over the first d_1 arguments and the second, Q^{d_2}, over the last d_2 arguments of a multivariate function g. Then the d-dimensional lth order of the sparse Smolyak quadrature, denoted by $Q_l^{(d)}f$, is defined recursively as

$$Q_l^{(d)}f = \sum_{i=1}^{l}\left(Q_i^{(1)}-Q_{i-1}^{(1)}\right)\times Q_{l-i+1}^{(d-1)}f. \quad (2.19)$$

With this multidimensional quadrature, we can approximate the inner product of the source term ω_F by expressing it as a function of $\boldsymbol{m}(\boldsymbol{\xi})$ and $\boldsymbol{n}(\boldsymbol{\xi})$ obtained from

https://doi.org/10.1017/jfm.2014.96 Published online by Cambridge University Press

the polynomial expansions, (2.14) and (2.15). This gives $\omega_F(\boldsymbol{\xi})$, and the inner product $\langle \omega_F(\boldsymbol{\xi}) \mid \Psi_k(\boldsymbol{\xi}) \rangle$ is approximated by

$$\langle \omega_F(\boldsymbol{\xi}) \mid \Psi_k(\boldsymbol{\xi}) \rangle \approx Q_l^{(d)} \left(\omega_F(\boldsymbol{\xi}) \Psi_k(\boldsymbol{\xi}) \right), \tag{2.20}$$

where the lth-order quadrature $Q_l^{(d)}$ is used to integrate over the d-dimensional sample space variable $\boldsymbol{\xi}$.

Use of the Smolyak quadrature yields, for smooth functions f, exponential convergence of the numerical error with respect to the order l of the quadrature $Q_l^{(d)} f$. Furthermore, since it is based on only those points of the d-dimensional product of the univariate quadratures $Q_l^{(1)}$ which yield product quadratures of order l or less (whereas a standard d-dimensional product of the univariate quadratures yields product quadratures of order ld), the Smolyak quadrature $Q_l^{(d)} f$ involves evaluation at considerably fewer points than does a simple product of univariate quadratures. To match the accuracy of the Smolyak quadrature to that of the PCE, we use the same order for both: for the seventh-order, five-dimensional case considered below, a simple product of the seventh-order, 15-point nested univariate quadratures would require $15^5 = 759\,375$ points, whereas the Smolyak quadrature given by (2.19) requires only 1743 points.

3. Simulation

Combustion instability was studied over a range of operating conditions for a 10-injector design by Sirignano & Popov (2013). With varying mixture ratio or mass flow, three zones corresponding to different types of stability were found: stable operation under any perturbation; linear (spontaneous) instability with infinitesimal perturbation (noise), resulting in a nonlinear limit-cycle oscillation; and an operating zone where triggering occurs with a disturbance above a threshold magnitude, leading to a nonlinear limit-cycle oscillation, while a perturbation below the threshold decays. Here, our stochastic analysis will focus on this last operating regime where triggering action is possible.

The present simulation uses a cylindrical chamber of axial length $L = 0.5$ m and radius $R = 0.14$ m, with 10 injectors: one at the centre of the chamber, three at $r = R/2$, evenly spaced at angles of $2\pi/3$, and six at $r = 3R/4$, evenly spaced at angles of $\pi/3$. Each injector consists of two concentric pipes: the inner one, with a radius of 0.898 cm, serves as the oxidizer inlet, and the outer one, with a radius of 1.1 cm, serves as the fuel inlet, allowing fuel and oxidizer inflow in stoichiometric proportions. The injector configuration is shown in figure 1(*a*).

The fuel and oxidizer in the present simulation are, respectively, gaseous-phase methane and oxygen, entering the combustion chamber at 400 K with an axial velocity of 200 m s^{-1}. Using a value of 0.115 for the ratio between the nozzle throat area and the combustion chamber cross-sectional area results in a steady-state operational pressure of 200 atm and a steady-state temperature of 2000 K.

The solution is found in two forms and comparisons are made. Equations (2.16) and (2.17) for the coefficients of the Legendre polynomials for the PCE approach are numerically integrated. Then the primitive variables, e.g. pressure and velocity, are constructed. Equations (2.1)–(2.9), the original PDEs governing the evolution of the primitive variables, are also integrated directly, following Sirignano & Popov (2013). The calculations are performed for a reasonable sampling over the ranges of the several random variables. Comparisons of the two results are made for

https://doi.org/10.1017/jfm.2014.96 Published online by Cambridge University Press

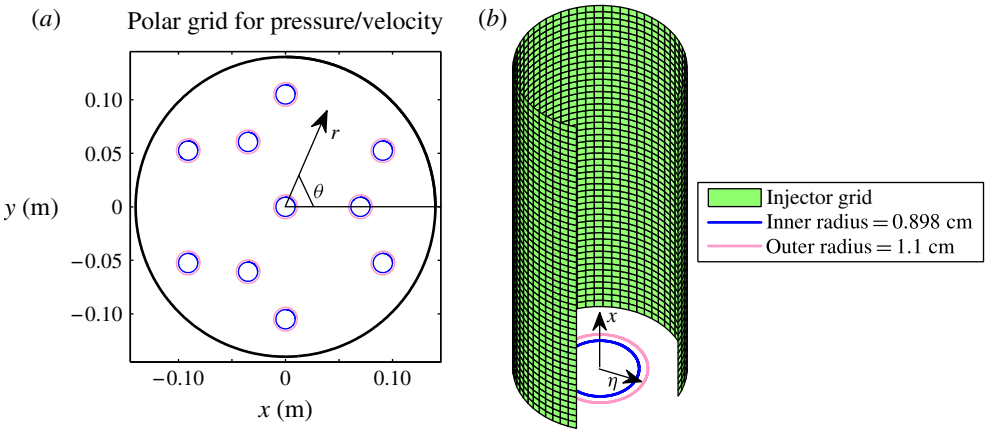


FIGURE 1. (Colour online) Illustration of the two types of grid used in the computational procedure. (*a*) The pressure and velocity equations are solved on a polar grid in r–θ coordinates. (*b*) The injector grids are axisymmetric cylindrical grids in x–η coordinates.

both the primitive variables and the probability functions that result from certain integrations over the sample sets. The direct solution of the original PDEs is sufficiently independent of mesh size and time step to be considered the 'exact solution' for benchmarking the PCE results. Errors in the PCE calculation of the primitive variables are examined for various choices of truncation of the PCE series. In addition, the direct simulations of the original PDEs are used for the realizations in a Monte Carlo simulation, which are compared to the efficiencies, i.e. computational cost versus accuracy, of the two approaches in prediction of the probabilities.

Some description of the physical behaviour, obtained using direct simulation of the original evolution equations, follows. Then, in §§ 3.1 and 3.2, two types of pulses examined for the calculations of the probability of triggering action are discussed.

The evolution equations for pressure and velocity, (2.1), (2.5) and (2.6), are solved using a second-order finite-difference procedure on a uniform polar grid, with the radial and azimuthal components of velocity staggered with respect to pressure. The evolution equations (2.7)–(2.9) for the scalars α, β and Y_F are solved on 10 disjoint two-dimensional cylindrical grids (neglecting field variations in the azimuthal variable), each co-axial with the axis of the respective injector. For more details on the solution procedure for the deterministic system, the reader is referred to Sirignano & Popov (2013).

With this set-up for a deterministic simulation with known initial conditions, a stable limit cycle was found in the form of a travelling first tangential mode of peak-to-peak amplitude 155 atm. Similarly, the triggering initial perturbation is a travelling first tangential mode of amplitude above 20 atm; for initial perturbations of smaller amplitude, decay towards the steady-state operational conditions was found. This is illustrated in figure 2, which shows pressure contour plots for a first tangential mode perturbation, together with the final pressure field once a limit cycle has developed.

Figure 3 plots the final amplitude of the solution against the amplitude of the initial perturbation. A triggered instability can be observed, with solutions of amplitude above 20 atm growing to 155 atm and solutions of peak-to-peak amplitude below 20 atm decaying to zero.

https://doi.org/10.1017/jfm.2014.96 Published online by Cambridge University Press

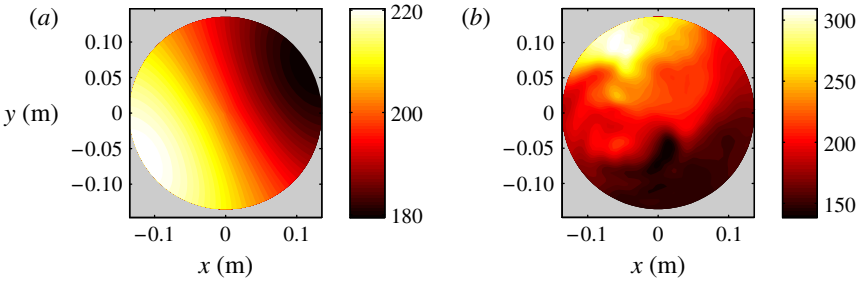


FIGURE 2. (Colour online) Pressure contours for (*a*) the initial disturbance and (*b*) the final spinning wave limit cycle.

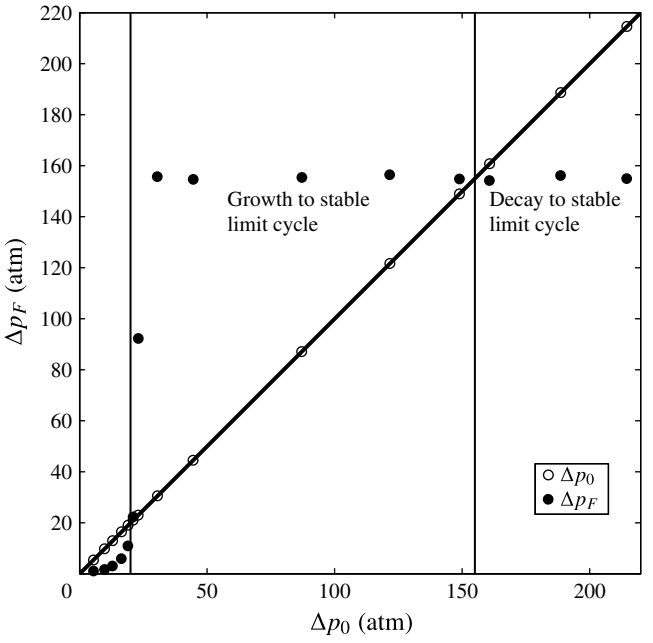


FIGURE 3. Final peak-to-peak amplitude, Δp_F, versus the initial amplitude of the perturbation, Δp_0.

Figure 4(*a*) shows phase plots of pressure and its time derivative for the point on the wall at $\theta = 3\pi/4$. Two solutions, with initial amplitudes 18 and 140 atm, are presented. The solution with initial amplitude above 20 atm is attracted to a stable limit cycle, whereas the solution with initial amplitude below 20 atm decays. An unstable limit cycle is present in the region between 18 and 22 atm. This is an example of a linearly stable system with a triggered nonlinear instability. When the injector mass flows of both fuel and oxidizer are increased, the LPRE becomes unconditionally unstable (figure 4*b*), with every perturbation growing to a limit cycle. On the other hand, for a very lean fuel-to-oxidizer mass flow ratio (figure 4*c*), the system becomes unconditionally stable, with all perturbations decaying towards the steady-state operating conditions.

For this configuration, it was shown that the same nonlinear limit-cycle oscillation could result from different disturbances (Sirignano & Popov 2013). An initial pressure

https://doi.org/10.1017/jfm.2014.96 Published online by Cambridge University Press

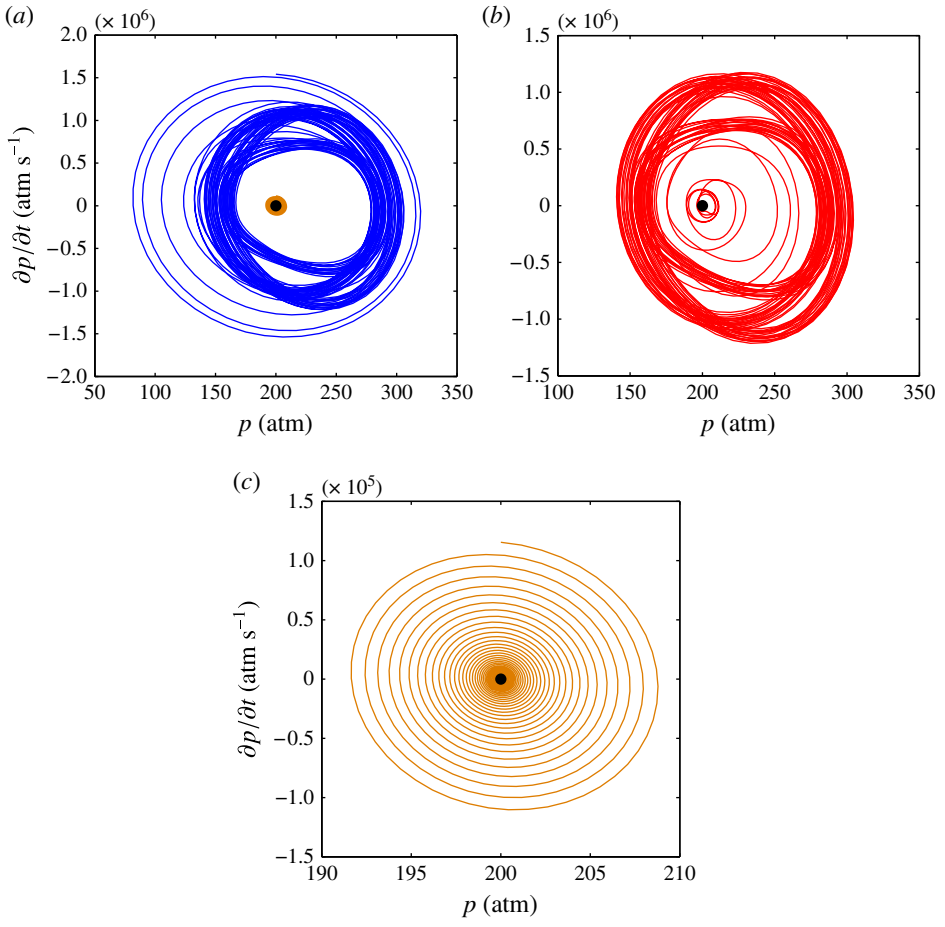


FIGURE 4. (Colour online) Phase plots of $\partial p/\partial t$ versus p at the position on the chamber wall where $\theta = 3\pi/4$, for three possible cases. (*a*) Present configuration, with a stable equilibrium at the operating conditions and a triggered instability: a solution with initial amplitude below 20 atm decays to the equilibrium, whereas a solution with initial amplitude above 20 atm is attracted to a stable limit cycle. (*b*) A configuration with increased injector mass flow, which is unconditionally unstable: any perturbation grows to a limit cycle. (*c*) A configuration with a lean fuel-to-oxidizer mass flow, which is unconditionally stable: every perturbation decays to the steady state.

variation identical to the linear profile for the first tangential acoustic mode could trigger the 155 atm peak-to-peak limit-cycle amplitude if that initial amplitude were greater than 20 atm. A forcing function consisting of a Gaussian travelling pulse applied for an extremely brief period (a numerical approximation to a delta function) with magnitude greater than 40 atm could also result in the same 155 atm limit cycle.

If the orientation of the pulse's direction of travel were modified, changes in the limit cycle could result. For example, Sirignano & Popov (2013) showed that a first radial mode could superimpose on the first tangential mode of oscillation. Thus, the details of the limit-cycle behaviour can have some dependence on the disturbance. Therefore, the limit-cycle parameters are random variables as well, inasmuch as they

https://doi.org/10.1017/jfm.2014.96 Published online by Cambridge University Press

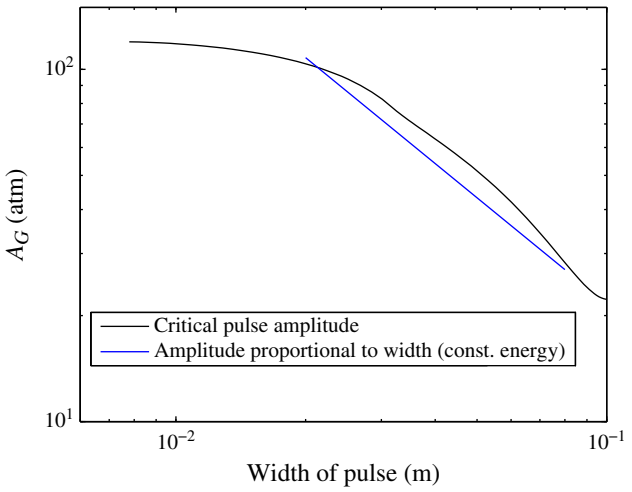


FIGURE 5. (Colour online) Critical amplitude required for triggering of the first tangential mode limit cycle by a single pulse.

are non-trivial functions of the disturbance. Nevertheless, a given disturbance produces in a deterministic fashion a unique limit cycle.

A set of deterministic calculations determines that for a single pressure pulse of width W_G, initially travelling parallel to the chamber wall in the azimuthal direction, there exists a critical pressure amplitude A_G, below which the pulse will decay and above which it will trigger growth to the spinning first tangential limit cycle of amplitude 155 atm found in Sirignano & Popov (2013). The value of this critical amplitude is plotted in figure 5 as a function of the pulse width.

Figure 5 shows that for most of the parameter range (from 2 to 8 cm) including the pulse widths of interest, the critical value of A_G scales as W_G^{-1}, i.e. the energy of the pulse at critical amplitude is independent of W_G. Here, we shall consider a pair of pulses whose energy is half the critical energy for a single pulse and examine the conditions under which the combination of these pulses triggers growth to the limit cycle.

In this study, we explore a parameter space of stochastic, localized pressure perturbations of two different kinds: Gaussian travelling pulses and dipoles.

3.1. *A pair of travelling Gaussian pulses*

This first set of simulations determines a combination of two travelling pulses that can trigger growth to a limit cycle, although each pulse by itself is too weak to trigger a limit-cycle oscillation. The initial pressure pulse added to the steady-state pressure of 200 atm has the form

$$p(r, \theta, t=0) = q(r, \theta, t=0), \tag{3.1}$$

$$\frac{\mathrm{d}p}{\mathrm{d}t}(r, \theta, t=0) = \frac{\mathrm{d}q}{\mathrm{d}t}(r, \theta, t=0), \tag{3.2}$$

$$q(r, \theta, t) = A_G \exp\left(-\frac{\|z - z_1(t)\|^2}{w_G^2/2}\right), \tag{3.3}$$

https://doi.org/10.1017/jfm.2014.96 Published online by Cambridge University Press

with

$$\boldsymbol{z} = r\cos(\theta)\boldsymbol{i} + r\sin(\theta)\boldsymbol{j}, \tag{3.4}$$

$$\boldsymbol{z_1}(t) = (r_1\cos(\theta_1) - a_0 t\sin(\theta_1+\theta_2))\,\boldsymbol{i} + (r_1\sin(\theta_1) + a_0 t\cos(\theta_1+\theta_2))\,\boldsymbol{j}, \tag{3.5}$$

where r_1, θ_1 and θ_2 are parameters governing the initial location and direction of travel, with their values set to $r_1 = 0.09$ m, $\theta_1 = \pi$ and $\theta_2 = 0$. Thus, the first pulse has amplitude A_G and width w_G, and it is initially travelling counterclockwise at the speed of sound. We shall perform two separate PCE simulations for two sets of values for the parameters A_G and w_G: the first has $w_G = 3.5$ cm and $A_G = 50$ atm, and the second has $w_G = 2.5$ cm and $A_G = 70$ atm. For both of these parameter sets, the amplitude of the first pulse on its own is insufficient to cause a limit cycle to develop; the critical amplitude for a single pulsed trigger is 70 atm for a pulse of width 3.5 cm and 98 atm for a pulse of width 2.5 cm. Therefore, this set of simulations will lead to the development of a limit cycle only when the second pulse, to be described presently, reinforces the first one.

The second pulse, with the same form as the first pulse, is introduced with a time delay of $T_S = \xi_1 \times 6 \times 10^{-3}$ s after the first pulse and is governed by (3.3), with the parameters in (3.5) defined by $r_1 = \xi_2 R$, $\theta_1 = -\pi + 2\pi\xi_3$ and $\theta_2 = 2\pi\xi_4$. The random variables $\xi_1, \ldots, \xi_4$ are independent and uniformly distributed on the interval [0, 1]; accordingly, to ensure spectral convergence of the error in the PCE approximation of (2.16), we choose $\Psi_k(\boldsymbol{\xi})$ to be the Legendre polynomials of degree up to seven in $\xi_1, \ldots, \xi_4$.

All of the uncertainty in this simulation is contained in the timing, location and direction of travel of the second pulse. This is intentional: in order to keep the pressure field smooth in time, the PCE simulation starts with the introduction of the second pulse at time T_S, with the initial fields caused by the first pulse up to that time being obtained from a pre-computed deterministic simulation. The PCE simulation is then run from time T_S until time $T_F = T_S + 6 \times 10^{-3}$ s, which corresponds to approximately 12 periods of the chamber's first tangential mode; the period of this mode is equal to $\tau_F = 4.87 \times 10^{-4}$ s.

3.2. *A pressure dipole*

Using the same combustion chamber conditions as for the two-pulse PCE calculations, we also perform simulations for a pressure dipole defined as

$$p(x,y,t)_{t<T_D} = -A_D \times \exp\left(-\left(\frac{r_1}{0.0025\ \text{m}}\right)^2\right) \times \sin\left(\frac{2\pi t}{\tau_D}\right) + A_D \times \exp\left(-\left(\frac{r_2}{0.0025\ \text{m}}\right)^2\right) \times \sin\left(\frac{2\pi t}{\tau_D}\right), \tag{3.6}$$

$$r_1 = \left(\left(x + r_D + 0.005\ \text{m} \times \sin(\theta_D)\right)^2 + \left(y - 0.005\ \text{m} \times \cos(\theta_D)\right)^2\right)^{1/2}, \tag{3.7}$$

$$r_2 = \left(\left(x + r_D - 0.005\ \text{m} \times \sin(\theta_D)\right)^2 + \left(y + 0.005\ \text{m} \times \cos(\theta_D)\right)^2\right)^{1/2}, \tag{3.8}$$

where the dipole amplitude is $A_D = \xi_1 \times 100$ atm, the period of the dipole is $\tau_D = (0.3 + 1.4\xi_2)\tau_F$, the duration for the dipole perturbation is $T_D = 2\xi_3 \times \tau_F$, the dipole location is prescribed by $r_D = 0.14$ m $\times\, \xi_4$, and $\theta_D = \pi \times \xi_5$. Similar to the previous subsection, $\xi_1, \ldots, \xi_5$ are independent and uniformly distributed on [0, 1], and we use Legendre polynomials of up to seventh degree in $\xi_1, \ldots, \xi_5$ as the PCE basis functions $\Psi_k(\boldsymbol{\xi})$. Again, the simulation runs for 6×10^{-3} s, or approximately 12 periods of the first tangential mode.

https://doi.org/10.1017/jfm.2014.96 Published online by Cambridge University Press

4. Results

In this section, we explore perturbations that trigger the 155 atm limit cycle seen previously. In the deterministic study of this configuration (Sirignano & Popov 2013), the first tangential mode limit cycle was discovered when a first tangential mode of sufficient amplitude was input as the initial condition. On the other hand, initial perturbations of lower magnitude decayed with increasing time in the simulations performed by Sirignano & Popov (2013). Therefore, a reasonable way of deciding whether a solution will decay or develop towards a limit-cycle oscillation for a given value of $\boldsymbol{\xi}$ is to test whether the peak-to-peak amplitude of the pressure field at the end of the simulation is above half of the deterministic limit-cycle amplitude. Specifically, for a given $\boldsymbol{\xi}$, we define $I(\boldsymbol{\xi})$ by the formula

$$M(\boldsymbol{\xi}) = \max_{r,\theta} \left(\max_{T_F \geqslant t \geqslant T_F - \tau_F} p\,(r, \theta, t, \boldsymbol{\xi}) - \min_{T_F \geqslant t \geqslant T_F - \tau_F} p\,(r, \theta, t, \boldsymbol{\xi}) \right), \tag{4.1}$$

$$I(\boldsymbol{\xi}) = \begin{cases} 1 & \text{for } M(\boldsymbol{\xi}) > 77.5 \text{ atm}, \\ 0 & \text{for } M(\boldsymbol{\xi}) \leqslant 77.5 \text{ atm}. \end{cases} \tag{4.2}$$

In the definition of $M(\boldsymbol{\xi})$, we take the maxima and minima over all r, θ and over all $t \in [T_F - \tau_1, T_F]$. We choose this interval, rather than just fixing $t = T_F$, to ensure that a meaningful value of $M(\boldsymbol{\xi})$ is obtained in the case where the limit cycle for a given $\boldsymbol{\xi}$ is a standing wave with oscillating peak-to-peak magnitude.

The random variable $I(\boldsymbol{\xi})$ can be viewed as an indicator function for the cases where the chamber perturbation grows to a first-tangential-mode limit cycle. This is confirmed via examination of the (r, θ) spectrum of 10 000 solutions for random $\boldsymbol{\xi}$ with $I(\boldsymbol{\xi}) = 1$: in all cases, a minimum of 82 % of the energy of $p(r, \theta, t > T_F - \tau_1)$ is contained in the first tangential mode of the (r, θ) spectrum. For these 10 000 solutions, the sensitivity of $I(\boldsymbol{\xi})$ is also tested for the choice of the 77.5 atm threshold and the length of 12 cycles for the time window of the simulation. There is some, but not great, sensitivity to these two parameters due to the fact that the finite simulation time means that marginal cases in the sample space have not converged to their ω-set by the end of the simulation. In particular, for those of the 10 000 simulations which yield marginal values of $M(\boldsymbol{\xi}) \in (35, 120)$ atm, the simulation is run for 10 times the regular period (i.e. 120 cycles of oscillation), which is sufficient for all cases to either decay or get attracted to the limit cycle of 155 atm. A simulation is then deemed misclassified based on the criterion of (4.1) and (4.2) if $I(\boldsymbol{\xi}) = 1$ for a decaying perturbation (false positive) or if $I(\boldsymbol{\xi}) = 0$ for a perturbation which grows to the limit cycle (false negative). The overall fraction of misclassified simulations among the 10 000 is 0.83 % (all false negatives), which is small enough to justify the effectiveness of the criterion defined in (4.2), albeit the threshold choice could be further optimized. These findings support the analysis approach for the combustion instability considered, and although, in principle, it can be useful for other applications, no claim is made about its universality.

We examine the marginal probability density functions (PDFs) of the random variable $I(\boldsymbol{\xi})$ in one or two of the random variables ξ_i, defined as follows:

$$I_{\Xi_i}(\xi_i) \equiv \int I(\boldsymbol{\xi})\, \mathrm{d}\xi_1 \cdots \mathrm{d}\xi_{i-1}\, \mathrm{d}\xi_{i+1} \cdots \mathrm{d}\xi_n, \tag{4.3}$$

$$I_{\Xi_i \Xi_j}(\xi_i, \xi_j) \equiv \int I(\boldsymbol{\xi})\, \mathrm{d}\xi_1 \cdots \mathrm{d}\xi_{i-1}\, \mathrm{d}\xi_{i+1} \cdots \mathrm{d}\,\xi_{j-1} \mathrm{d}\xi_{j+1} \cdots \mathrm{d}\xi_n, \tag{4.4}$$

https://doi.org/10.1017/jfm.2014.96 Published online by Cambridge University Press

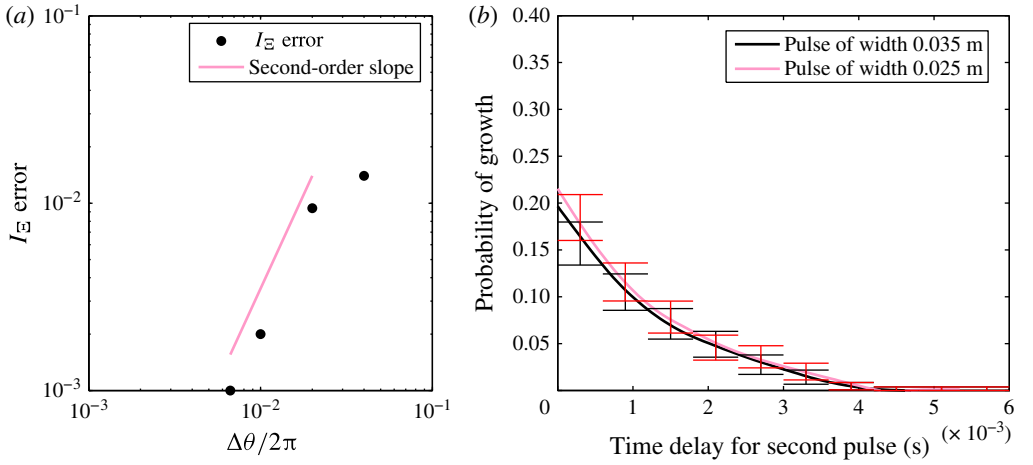


FIGURE 6. (Colour online) (*a*) Maximal error in the computed value of $I_{\Xi_1}(\xi_1)$ as a function of the grid cell size. (*b*) Probability of growth as a function of the time delay between the two pulses.

where n is the number of random variables and $i < j$. Note that the above equation is a valid definition of a marginal PDF, as the sample space in the present study is an n-dimensional unit cube with a uniform probability measure. The integrations in (4.3) and (4.4) are performed numerically, via a Smolyak grid quadrature similar to the one used in the evaluation of the nonlinear terms of the PCE evolution equation.

Before presenting the PCE results, we verify the grid and time-step convergence of the PDE solution, for different grid and time-step resolutions and the same seventh-degree PCE; by doing this, we shall establish that the numerical errors due to the grid size and time step are small compared with the PCE approximation errors. Setting $\xi_2 = 0.5$ and $\xi_3 = 0.25$ for the test case described in § 3.2, we have a computationally cheaper test case, with a three-dimensional sample space, on which a set of calculations are made using grids of size 12×25, 25×50, 50×100, 75×150 and 150×300 in the r and θ directions. The time step is kept proportional to the grid size, with $\Delta t = 7.5 \times 10^{-7}$ s for the 50×100 r–θ grid. Similarly, the size of each of the 10 injector grids is kept proportional to the size of the r–θ grid: for the 50×100 r–θ grid, the size of the x–η injector grid is 40×40. Figure 6 plots the maximal error in the calculated value for $I_{\Xi_1}(\xi_1)$ as a function of the grid spacing in the θ direction; the finest grid solution is used as the exact answer.

The solutions are seen to converge in a second-order fashion, with the 50×100 solution (which is used in the rest of the paper) yielding a maximal error of 0.002 in $I_{\Xi_1}(\xi_1)$, well below the PCE approximation error, which is discussed in the remainder of this section.

4.1. *Results for a pair of subthreshold travelling pulses*

We first examine the effect of the time delay between the two pulses. Two sets of calculations are performed using pulses of width 2.5 and 3.5 cm with the same L^2 norm, equal to 0.707 of the critical value. Figure 6 plots, for these two cases, the value of the marginal PDF $I_{\Xi_1}(\xi_1)$ as a function of the time delay corresponding to a given value of ξ_1, which is the probability of growth as a function of the time delay.

https://doi.org/10.1017/jfm.2014.96 Published online by Cambridge University Press

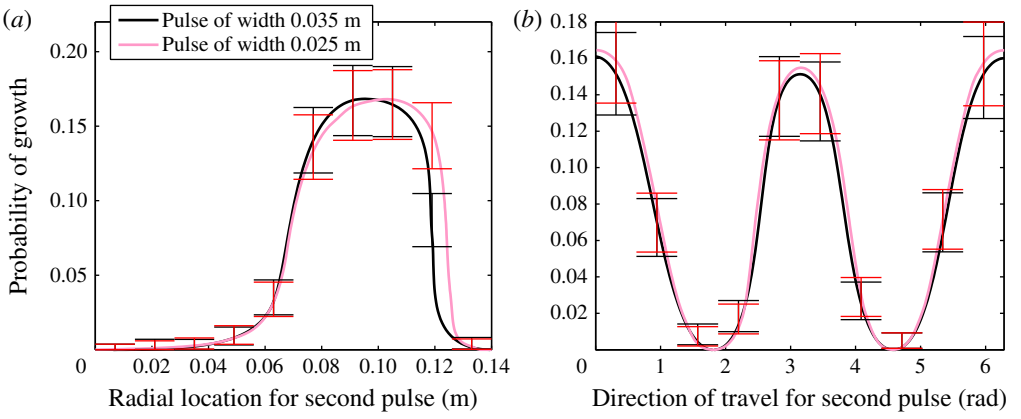


FIGURE 7. (Colour online) (*a*) Probability of growth as a function of the radial position of the second pulse. (*b*) Probability of growth as a function of the direction of travel of the second pulse.

The results are fairly intuitive, with the probability of growth decreasing as the time delay increases, due to the fact that the first pulse is subcritical and decays on its own. For the test case in which the two pulses have the same L^2 norm but a lower width of 2.5 cm, the marginal PDF and hence the overall probability of growth to a limit cycle are higher. In this and the following plots, Monte Carlo 95 % confidence intervals for the average value of the marginal PDF in the 10 bins are superimposed on the PCE curves, as a means of validating the accuracy of the PCE results. Later, a comparison of computational costs of the Monte Carlo and PCE methods will be made.

Figure 7 presents the probability of growth as a function of the radial location of the second pulse, which corresponds to the marginal PDF of $I_{\Xi_2}(\xi_2)$. The largest probability is observed near a radial location of $r = 0.1$ m for the second pulse, with a drop-off to zero for values at the low and high ends of the interval. For low values of r, this can be explained by the fact that the second pulse passes close to the centre of the chamber, which tends to excite a standing wave instability, whereas the first pulse, starting out near the wall and moving tangentially, excites a spinning wave instability.

For high values of the initial radial location of the second pulse, the drop in growth probability can be explained by the fact that part of the Gaussian profile of this pulse lies outside the domain, and so the overall L^2 norm of the second pulse is reduced; this is also the reason for the overall larger probability of growth for pulses of width 2.5 cm, as they are left without truncation for larger values of r. While the energy of the pulse is reduced, the truncated Gaussian function is still smooth in the computational domain, and hence the PCE smoothness convergence conditions are satisfied.

Figure 7 also presents the probability of growth as a function of the direction of travel of the second pulse initially, counterclockwise relative to the unit azimuthal vector at the initial location. The highest probability of growth occurs when the second pulse is travelling tangentially in the counterclockwise direction, similarly to the first pulse, with a lower probability at π, when the two are travelling in opposite tangential directions, and a drop to zero at $\pi/2$ and $3\pi/2$, where the second pulse is travelling radially and passes close to the centre of the domain. That is, since both pulses have subthreshold magnitudes, in a pair they can only cause growth when

https://doi.org/10.1017/jfm.2014.96 Published online by Cambridge University Press

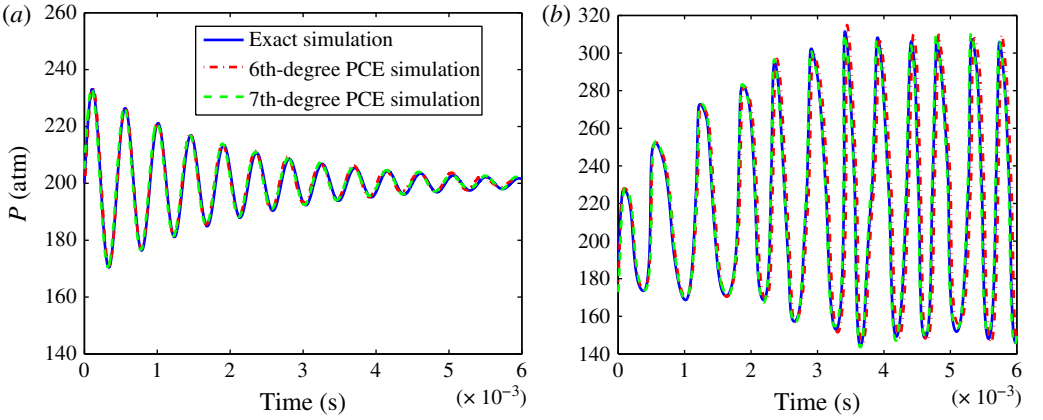


FIGURE 8. (Colour online) Comparison of the pressure versus time curves for a fixed point at $r = R, \theta = 3\pi/4$ generated by the sixth- and seventh-degree PCE simulations with a deterministic solution of the original differential equations for the same value of $\boldsymbol{\xi}$: (*a*) a solution attracted to a limit cycle; (*b*) a decaying solution.

there is considerable overlap in their trajectories of travel. Thus, since the first pulse travels in a tangential direction, the second pulse is more likely to lead to a limit cycle when it also travels in a tangential direction.

4.2. *Results for an oscillating dipole*

Prior to analysis of the probability of growth, we validate the PCE simulation by comparing the calculated PCE pressure at $r = R, \theta = 3\pi/4$ with the pressure calculated from a deterministic simulation for the same value of $\boldsymbol{\xi}$. Figure 8 shows results for two cases, one in which there is growth to the limit cycle and one in which there is decay. As can be seen, the sixth- and seventh-degree PCE simulations have sufficiently converged to the true solution.

For a more general analysis over the entire sample space, we calculate, for each of the 10 000 values of $\boldsymbol{\xi}$ corresponding to the Monte Carlo solutions, the average difference between the PCE solution for that value of $\boldsymbol{\xi}$ and the Monte Carlo sample. Figure 9 plots, for the PCE simulations of degree 1–7, the mean L^2 error at the end of the simulation, defined as

$$\varepsilon_{L^2} = \mathrm{Mean}_{\xi} \left\langle \frac{\left(\int \left(p^{PCE}(r, \theta, t, \boldsymbol{\xi}) - p(r, \theta, t, \boldsymbol{\xi}) \right)^2 r \, \mathrm{d}r \, \mathrm{d}\theta \, \mathrm{d}t \right)^{1/2}}{\left(\int \left(p(r, \theta, t, \boldsymbol{\xi}) - 200 \text{ atm} \right)^2 r \, \mathrm{d}r \, \mathrm{d}\theta \, \mathrm{d}t \right)^{1/2}} \right\rangle, \tag{4.5}$$

where $p^{PCE}(r, \theta, t, \boldsymbol{\xi})$ and $p(r, \theta, t, \boldsymbol{\xi})$ are, respectively, the PCE solution and the exact solution for pressure at a given value of $\boldsymbol{\xi}$. Also plotted in that figure is the fraction of Monte Carlo samples in which the value of $I(\boldsymbol{\xi})$ from the PCE simulation differs from the value obtained using the exact solution. With increasing PCE simulation degree, convergence with respect to both of these measures of error can be observed in figure 9.

In addition, figure 9 presents the probability of growth as a function of the dipole peak-to-peak magnitude. As can be expected, for small dipole magnitudes the probability of growth is small. We identify a region of high sensitivity between 40

https://doi.org/10.1017/jfm.2014.96 Published online by Cambridge University Press

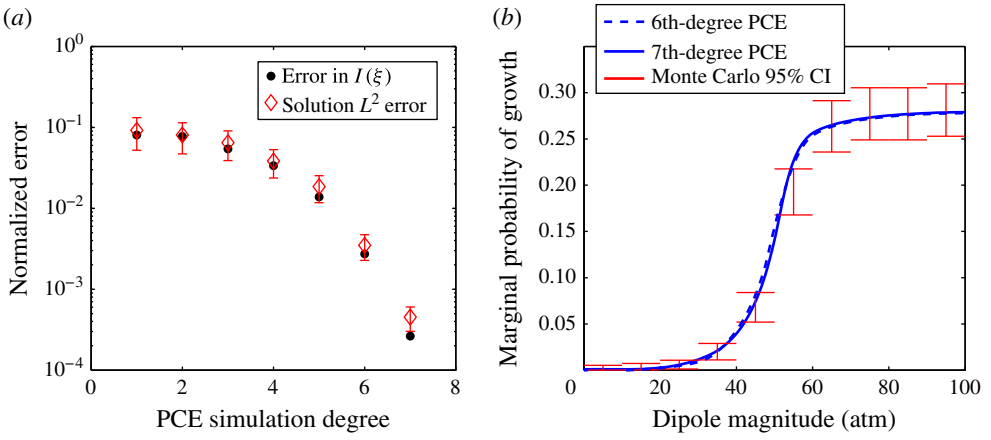


FIGURE 9. (Colour online) (*a*) Convergence plots for increasing PCE degree, based on the average error over the values of $\boldsymbol{\xi}$ for the 10 000 Monte Carlo samples: both the error with respect to the L^2 norm of the difference between the PCE and the exact solution (diamonds) and the error in the calculation of $I(\boldsymbol{\xi})$ are shown, normalized respectively; the bars indicate the variance in the L^2 error over the samples. (*b*) Probability of growth as a function of the dipole magnitude; the bars indicate the Monte Carlo 95 % confidence intervals.

and 60 atm, in which the probability of growth increases five-fold. Above 60 atm the marginal PDF curve levels off to a value of approximately 0.28.

Similarly to the previous subsection, Monte Carlo confidence intervals are calculated for the overall probability of growth when the abscissa variable (in this case the dipole magnitude) is in each of 10 bins uniformly dividing its range. As can be seen in this figure and the next four, the Monte Carlo confidence intervals overlap the PCE marginal probability curves.

For this case, two PCE simulations are performed, one with polynomial terms of up to seventh degree (solid line) and one with polynomial terms of up to sixth degree (dashed line). Figures 9–11 show that the difference between the sixth- and seventh-degree PCE simulations is small; this indicates that the PCE truncation error for the seventh-degree simulation, which is comparable in magnitude, is much smaller than the width of the confidence intervals obtained from the traditional Monte Carlo approach.

Figure 10(*a*) presents the probability of growth as a function of the ratio τ_D/τ_F between the dipole period τ_D and the period of the first tangential acoustic mode, τ_F. The results indicate a high probability of growth near $\tau_D/\tau_F = 1$; this ratio decreases when τ_D is considerably smaller or greater than τ_F. Thus, the system is sensitive to the frequency of the perturbation, and the probability of triggering is small for perturbations whose frequency differs considerably from that of the first tangential mode. This result is to be expected because instability should be more likely if the pulsing is commensurate with the character of the resonant modes.

Figure 10(*b*) shows the probability of growth as a function of T_D/τ_F, the dipole duration normalized by the period of the first tangential mode. A distinction is made between standing and spinning first tangential mode limit cycles. The former are excited when T_D is an even positive multiple of $\tau_F/2$, and the latter when T_D is an odd positive multiple of $\tau_F/2$. This is caused by a tendency of the dipole to excite,

https://doi.org/10.1017/jfm.2014.96 Published online by Cambridge University Press

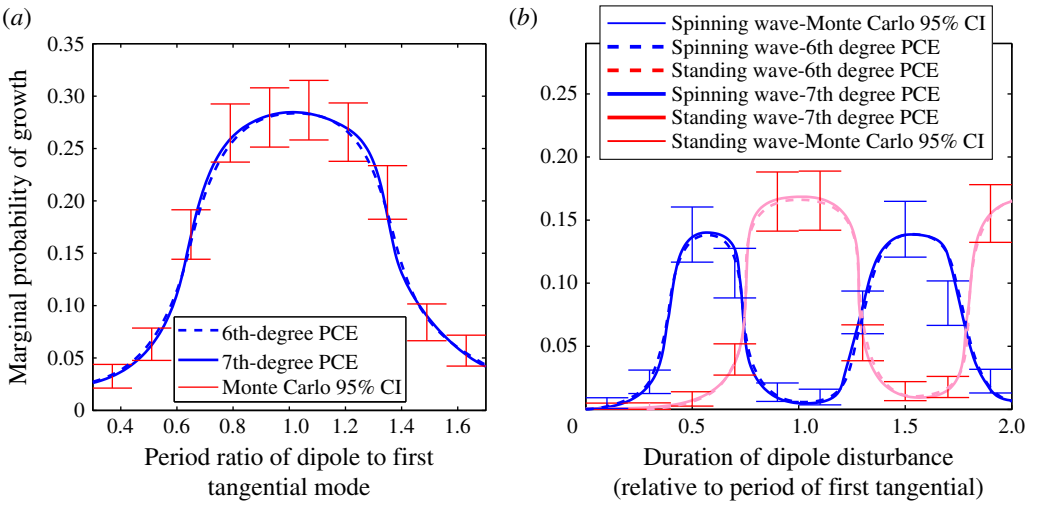


FIGURE 10. (Colour online) (*a*) Probability of growth as a function of the ratio between the dipole period and the period of the first tangential mode. (*b*) Probability of growth as a function of the dipole duration, normalized by the period of the first tangential mode.

over each half-period, a spinning wave travelling in the direction from positive to negative pressure, so that for $T_D \approx \tau_F$ and $T_D \approx 2\tau_F$ we get, respectively, one pair and two pairs of spinning waves travelling in opposite directions, resulting in a standing wave. Another interesting feature of the marginal PDFs shown in figure 10 is that standing wave limit cycles occur with greater probability, since a spinning wave is most highly excited by a dipole that is oriented tangentially and located near the edge of the domain. This result might change if the combustion process were sensitive to transverse velocity as well as pressure.

Figure 11(*a*) displays the probability of growth as a function of the dipole radial location. This probability increases for radial locations that are closer to the chamber wall. Similar to the above discussion, this occurs because either a spinning wave or a standing wave limit cycle may be excited. The former can only be excited by a dipole whose axis is oriented tangentially, for which it is necessary that the dipole location be away from the centre. On the other hand, a standing wave limit cycle can develop from dipoles of both radial and tangential orientations, and thus the probability of excitation of a limit cycle is greater for dipoles closer to the chamber wall.

The same basic mechanism explains the results shown in figure 11(*b*), which presents the probability of growth as a function of the dipole orientation, i.e. its angle with respect to the chamber tangent. The triggering probability is greater for angles close to 0 and π, which allow for the excitation of both standing and spinning waves, with the dipole's duration making the difference between a standing and a spinning wave. For dipole angles close to $\pi/2$, however, only standing waves are possible and thus the probability is lower.

Figures 12–13 examine the joint dependence on two of the random variables of the probability of growth. Figure 12(*a*) presents the probability of growth as a function of both the position and the orientation of the dipole. Again, we see a higher probability of growth for tangentially oriented dipoles and dipoles away from the domain's centre. For constant angular orientation near $\pi/2$, i.e. a radially oriented dipole, the probability of growth does not increase significantly with increasing radial location;

https://doi.org/10.1017/jfm.2014.96 Published online by Cambridge University Press

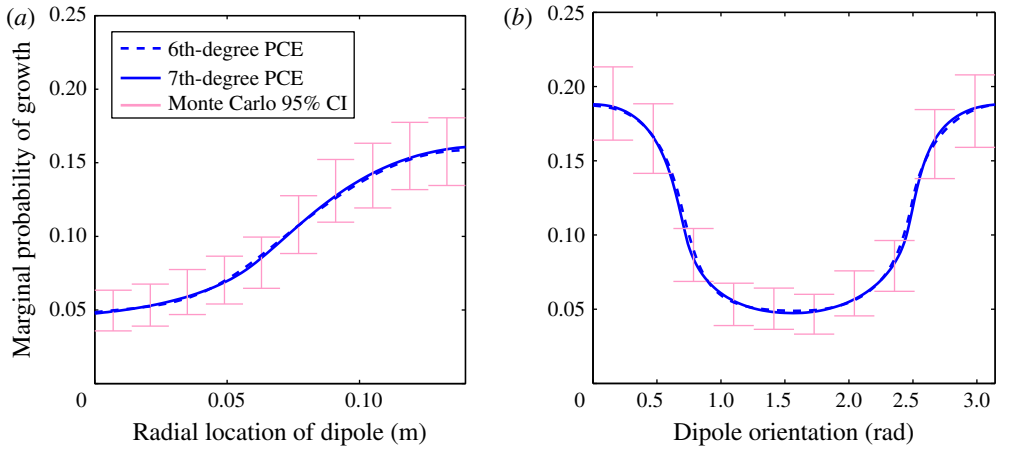


FIGURE 11. (Colour online) (*a*) Probability of growth as a function of the dipole radial location. (*b*) Probability of growth as a function of the dipole orientation.

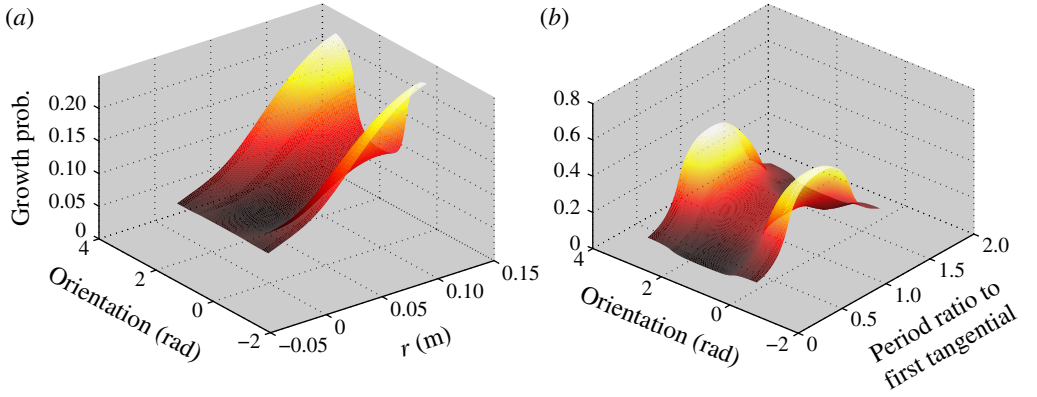


FIGURE 12. (Colour online) (*a*) Probability of growth as a function of the radial position and orientation of the dipole. (*b*) Probability of growth as a function of the dipole orientation and the ratio between the dipole period and that of the first tangential acoustic mode.

however, for an angular orientation near 0 or π, the probability increases considerably with increasing radial location. This occurs because these angular orientations allow for the excitation of a spinning wave limit cycle which, as previously mentioned, requires that the dipole be situated away from the centre of the chamber. For radial positions close to the centre, the plot shows that the results are less sensitive to the orientation, due to a high degree of rotational symmetry.

Figure 12(*b*) shows that there is no significant interaction between the dipole orientation and the ratio of the dipole's period to the period of the first tangential acoustic mode: the joint probability is closely approximated by the product of the one-dimensional marginal probabilities from figures 10 and 11. Since the dipole orientation affects the probability of growth via the excitation of either spinning or standing waves, this near-independence between orientation and period implies that the excitation of both spinning and standing waves is equally sensitive to the dipole period.

https://doi.org/10.1017/jfm.2014.96 Published online by Cambridge University Press

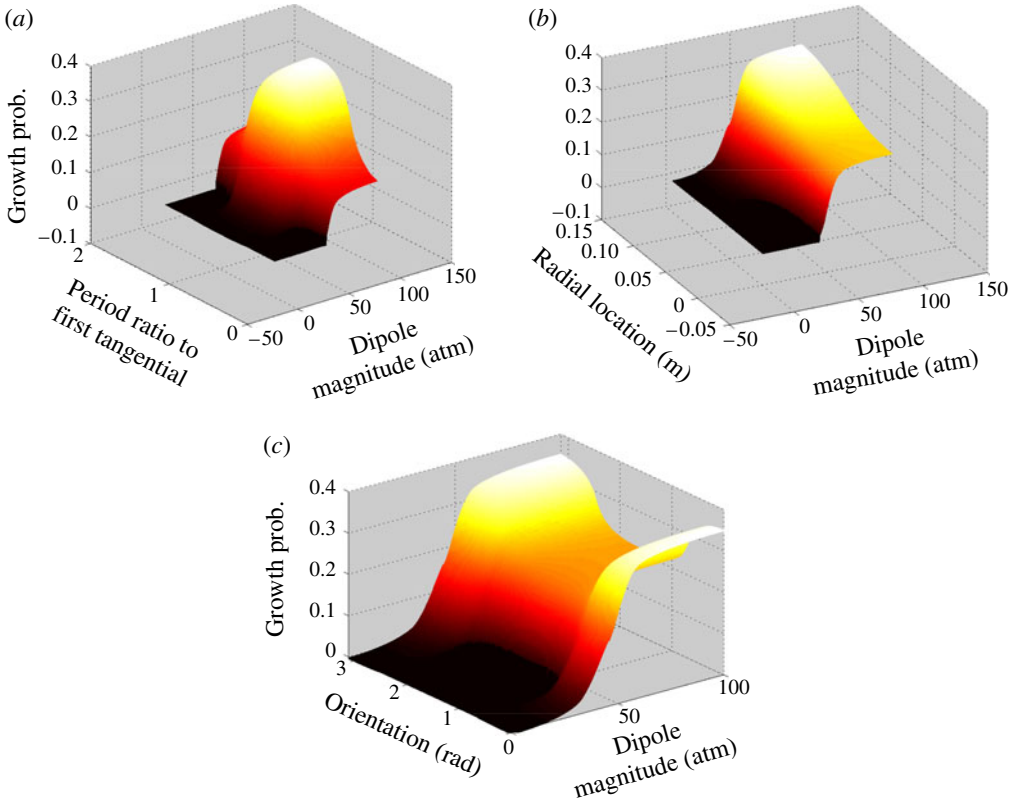


FIGURE 13. (Colour online) Probability of growth as a function of the dipole magnitude and: (*a*) the ratio of the dipole period to the period of the first tangential mode; (*b*) the dipole's radial location; and (*c*) the dipole's orientation.

Figure 13 plots the joint probabilities for dipole magnitude and three other parameters, namely the period, radial location and orientation of the dipole. All three plots exhibit the same behaviour, in that for each given value of the dipole period, radial location and orientation, there is a critical value for the dipole magnitude below which the probability of growth is zero. This result is due to the combustion chamber being linearly stable, so that there is a global minimum for the dipole magnitude below which perturbations decay regardless of their other characteristics, such as period and location. Additionally, figure 13 shows that for fixed values of the dipole's period, location and orientation, the probability of growth levels off above a certain value (approximately 60 atm) of the dipole magnitude. This indicates that above that magnitude, the difference between growth and decay is mostly due to the geometric and time parameters.

4.3. *Computational cost*

The advantage of the stochastic Galerkin procedure over a standard Monte Carlo approach to solving (2.12) and (2.13) lies in the fact that, for appropriately chosen polynomials $\Psi_k(\boldsymbol{\xi})$ (Legendre polynomials in the present simulation, due to $\boldsymbol{\xi}$ being uniformly distributed), the error in the approximation of (2.16) and (2.17) exhibits spectral convergence with respect to l (exponential convergence for solutions

https://doi.org/10.1017/jfm.2014.96 Published online by Cambridge University Press

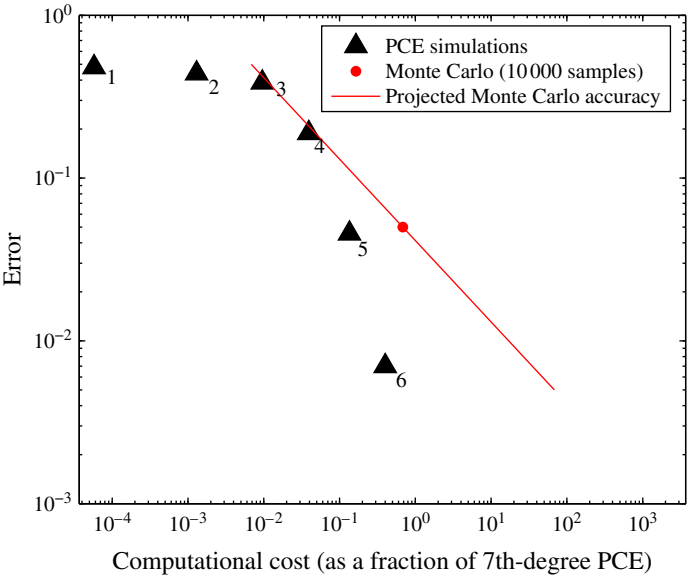


FIGURE 14. (Colour online) Computational efficiency plot comparison of the Monte Carlo and PCE approaches, based on the maximal error in the computed marginal probability of growth.

that are smooth in the uncertain parameters); see Xiu & Karniadakis (2002). The computational cost is modelled as being proportional to the total number of fields, which in the present case is $33 \times (P+1) = 33 \times (n+l)!/(n!\,l!)$. Therefore, this cost increases (for large values of l) as l^n, i.e. polynomially in l. On the other hand, a Monte Carlo approximation with N samples contains a random error proportional to $N^{-1/2}$, from which it follows that PCE will always have better computational accuracy than Monte Carlo simulation above a certain polynomial degree at the same computational cost. For the low-dimensional sample spaces used in the present study (either four or five dimensions), this level is within computing capabilities, as we shall soon see.

The computational cost of the Monte Carlo simulation, which involves 10 000 samples, is 186 CPU hours for the dipole simulations, whereas the cost of the seventh-degree PCE simulations is 272 CPU hours, and for the sixth-degree PCE simulations it is 109 CPU hours. While this may at first glance suggest that the Monte Carlo approach is more efficient, we note that the width of the Monte Carlo confidence intervals at the high-probability regions of the sample space is approximately 0.05, whereas the estimated error in the PCE-calculated marginal PDFs (from the difference between the seventh- and sixth-degree PCE dipole simulations) is less than 0.01 even at the regions of greatest sensitivity of the conditional PDFs.

Figure 14 is a computational efficiency plot for the PCE simulation: solutions with polynomial degrees of 1–5 have been computed in addition to the already discussed solutions of sixth and seventh degree, and the accuracy of the first- to sixth-degree solutions has been calculated with respect to the solution of degree seven. The machine used for all calculations was a 2.66 GHz Intel Q6700 quad-core workstation, running in serial. While the absolute computational cost will vary for different machines, the relative computational cost of the PCE and Monte Carlo procedures is expected to remain the same.

https://doi.org/10.1017/jfm.2014.96 Published online by Cambridge University Press

The error in the PCE simulation of degree five is considerable, almost as high as that of the Monte Carlo approximation, and higher by a factor of six than the error of the sixth-degree PCE simulation. This is the reason why the results from the sixth- and seventh-degree PCE simulations are used in this section to analyse the stability of the combustion chamber. A comparison is made with the 10 000-sample Monte Carlo simulation (for which the error is estimated as the width of the 95 % confidence intervals) and with the projected accuracy and computational cost of Monte Carlo simulations with a different number of samples. Figure 14 shows that, while the PCE and Monte Carlo approaches have similar computational efficiency for high error levels, PCE is considerably more efficient at lower error tolerances. The Monte Carlo statistical error converges as the inverse square root of the number of samples. Thus, to achieve the same accuracy as the sixth-degree PCE simulation via a Monte Carlo simulation would involve a computational cost which is approximately 17 times that of the seventh-degree PCE simulation.

Modelling the computational cost of the n-dimensional lth-order PCE expansion to increase proportionally to the number of its coefficients, i.e. as $(n+l)!/(n!\,l!)+1$, it is estimated that the PCE method would be more computationally efficient than the Monte Carlo approach up to nine-dimensional sample spaces, for the level of accuracy exhibited by the seventh-degree PCE simulations. A nine-dimensional seventh-order PCE simulation would then take 3900 CPU hours, whereas a Monte Carlo simulation with the 250 000 samples needed to achieve the same accuracy would take 4600 CPU hours.

5. Conclusions

A nonlinear wave model has been used to predict the triggering of transverse mode combustion instability in a liquid-propellant rocket engine. A combustion chamber with 10 co-axial injectors of oxygen and methane gas has been selected for detailed computations. For certain operating conditions, i.e. mass flow, mean chamber pressure and propellant mixture ratio, small disturbances to the steady-state operation of this system will decay with time, but disturbances above some threshold level will develop towards a limit-cycle oscillation. For operation in this bi-stable domain, random disturbances are applied and the probability of development towards the limit cycle is estimated using the PCE method.

The PCE stochastic approach for analysing the sensitivity of processes in a continuous medium with respect to uncertainty has been well established through several publications. While the PCE method has been used before to study nonlinear oscillations in lumped dynamical systems, to our knowledge, the first study of nonlinear oscillations in a distributed parameter system and, in particular, for a combustor is presented here. Favourable comparisons of the truncated PCEs for the physical variables, e.g. oscillating pressure, are made with the direct simulation of the original governing partial differential equations. The long-time PCE solution is shown to converge sufficiently rapidly and to produce an approximation capable of predicting a limit cycle accurately. Thus, the PCE method works well in giving an accurate and relatively inexpensive solution. The PCE method can produce comparable accuracy to the Monte Carlo method with more than one order of magnitude less computational cost.

The random disturbances are applied as forcing functions for brief durations. Two types of these functions are considered that provide an orientation as well as a magnitude: a travelling Gaussian pulse and an oscillating dipole. For the travelling

https://doi.org/10.1017/jfm.2014.96 Published online by Cambridge University Press

Gaussian pulse, it is shown that the two descriptive parameters can conveniently be collapsed to one parameter over a range of values. Two sequential Gaussian pulses with small difference in their orientations are able to trigger instability for a case where a single pulse falls below the threshold value. The parameters describing the pulses in our analysis are random variables. For both types of pulse, magnitude, orientation and location are defined as random variables. In addition, the repeated Gaussian pulse uses separations in space and time, and the dipole pulse has duration and frequency as random variables. The outcome of the pulse on the steady-state engine operation is the stochastic variable to be determined: stable recovery of the steady state or limit-cycle oscillation. The nature of the limit cycle can change for different random disturbances.

Sensitivity of the probability of triggering to each of the random variables is demonstrated. In certain situations where the energy of a pulse is insufficient to trigger a pulse, repeated pulsing of the same type closely spaced in time and location to the first pulse can trigger instability.

For the dipole simulation, the probability of growth is greatest when the dipole's frequency is close to that of the first tangential mode. The probability of growth increases monotonically with the dipole magnitude, with the greatest sensitivity being found in the 40–60 atm interval: below 40 atm the probability is almost zero, and it does not increase considerably above 60 atm. When the period of the dipole perturbation is close to an odd multiple of $\tau_F/2$, a tangential travelling wave limit cycle is triggered, and when the period is close to an even multiple of $\tau_F/2$, a standing wave limit cycle is triggered. Higher probability of growth is observed for dipoles located near the edge of the chamber and oriented tangentially, which are conditions necessary for the excitation of a spinning wave.

A foundation has been given for two future analytical developments. One is the replacement of abstract random disturbances by specific physical and chemical random behaviours, e.g. dysfunction of propellant injector flows or a rogue vortex structure perturbing the mixture ratio distribution, burning rate or allowed flow through the choked exit nozzle. The second possible extension of this work is the development of passive and active controls to reduce the likelihood of undesired triggered instabilities.

Acknowledgement

This research was supported by the Air Force Office of Scientific Research under Grant FA9550-12-1-0156 with Dr Mitat Birkan as the Program Manager.

REFERENCES

AWAD, E. & CULICK, F. E. C. 1986 On the existence and stability of limit cycles for longitudinal acoustic modes in a combustion chamber. *Combust. Sci. Technol.* **46**, 195–222.

BAR-YAM, Y. 1996 *Dynamics of Complex Systems*. Copernicus Books.

BERAN, P. S., PETTIT, C. L. & MILLMAN, D. R. 2006 Uncertainty quantification of limit-cycle oscillations. *J. Comput. Phys.* **217**, 217–247.

BHATIA, R. & SIRIGNANO, W. A. 1991 A one-dimensional analysis of liquid-fueled combustion instability. *J. Propul. Power* **7**, 953–961.

CAMERON, R. & MARTIN, W. 1947 The orthogonal development of non-linear functionals in series of Fourier–Hermite functionals. *Ann. Maths* **48**, 385–392.

CHORIN, A. J. 1970 Gaussian fields and random flow. *J. Fluid Mech.* **41**, 387–403.

CROCCO, L. & CHENG, S.-I. 1953 High frequency combustion instability in rockets with distributed combustion. In *Fourth Symposium (International) on Combustion* vol. 4, pp. 865–880.

CROCCO, L. & CHENG, S.-I. 1956 In *Theory of Combustion Instability in Liquid Propellant Rocket Motors* AGARDograph, vol. 8, Buttersworth.

https://doi.org/10.1017/jfm.2014.96 Published online by Cambridge University Press

CROCCO, L. & MITCHELL, C. E. 1969 Nonlinear periodic oscillations in rocket motors with distributed combustion. *Combust. Sci. Technol.* **1**, 147–169.

CROCCO, L. & SIRIGNANO, W. A. 1966 Effects of transverse velocity components on the nonlinear behavior of short nozzles. *AIAA J.* **4**, 1428–1430.

CROCCO, L. & SIRIGNANO, W. A. 1967 *Behaviour of Supercritical Nozzle Under Three-Dimensional Oscillatory Conditions* AGARDograph, vol. 117, North Atlantic Treaty Organization.

CULICK, F. E. C. 1994 Some recent results for nonlinear acoustics in combustion chambers. *AIAA J.* **32**, 146–169.

CULICK, F. E. C. 2006 *Unsteady Motions in Combustion Chambers for Propulsion Systems. (AGARDograph)*, vol. RTO-AG-AVT-039. North Atlantic Treaty Organization.

DELPLANQUE, J. -P. & SIRIGNANO, W. A. 1993 Numerical study of transient vaporization of an oxygen droplet at sub- and super-critical conditions. *Intl J. Heat Mass Transfer* **36**, 303–314.

DELPLANQUE, J. -P. & SIRIGNANO, W. A. 1996 Transcritical liquid oxygen droplet vaporization: effect on rocket combustion instability. *J. Propul. Power* **12**, 349–357.

DUVVUR, A., CHIANG, C. -H. & SIRIGNANO, W. A. 1996 Oscillatory fuel droplet vaporization: driving mechanism for combustion instability. *J. Propul. Power* **12**, 358–365.

FLANDRO, G., FISCHBACH, S. & MAJDALANI, J. 2007 Nonlinear rocket motor stability prediction: limit amplitude, triggering, and mean pressure shift. *Phys. Fluids* **19** (9), 94101–94116.

GHANEM, R. & SPANOS, P. D. 1990 Polynomial chaos in stochastic finite elements. *J. Appl. Mech.* **57**, 197–202.

GUÉZENNEC, N., MASQUELET, M. & MENON, S. 2012 Large eddy simulation of flame-turbulence interactions in a LOX-CH_4 shear coaxial injector. *50th AIAA Aerospace Sciences Meeting including the New Horizons Forum and Aerospace Exposition*. American Institute of Aeronautics and Astronautics.

HARRJE, D. & REARDON, F. 1972 Liquid propellant rocket combustion instability. *NASA Technical Report* SP-194. National Aeronautics and Space Administration.

HEIDMANN, M. F. & WIEBER, P. R. 1965 Analysis of *n*-heptane vaporization in unstable combustor with travelling transverse oscillations *NASA Technical Note* D-3424. National Aeronautics and Space Administration.

HIEN, T. & KLEIBER, M. 1997 Stochastic finite element modeling in linear transient heat transfer. *Comput. Meth. Appl. Mech. Engng* **144**, 111–124.

JACOB, E. J., FLANDRO, G. A., GLOYER, P. W. & FRENCH, J. C. 2010 Nonlinear liquid rocket combustion instability behavior using UCDM^{TM} process. In *46th AIAA/ASME/SAE/ASEE Joint Conference and Exhibit* vol. 3, pp. 2796–2805. American Institute of Aeronautics and Astronautics.

KNIO, O. M. & LE MAÎTRE, O. P. 2006 Uncertainty propagation in CFD using polynomial chaos decomposition. *Fluid Dyn. Res.* **38**, 616–640.

LIN, G., SU, C. H. & KARNIADAKIS, G. E. 2006 Predicting shock dynamics in the presence of uncertainties. *J. Comput. Phys.* **217**, 260–276.

LIU, N., HU, B. & YU, Z. W. 2001 Stochastic finite element method for random temperature in concrete structures. *Intl J. Solids Struct.* **38**, 6965–6983.

LE MAÎTRE, O., KNIO, O., NAJM, H. & GHANEM, R. 2001 A stochastic projection method for fluid flow. I. Basic formulation. *J. Comput. Phys.* **173**, 481–511.

LE MAÎTRE, O., REAGAN, M., NAJM, H., GHANEM, R. & KNIO, O. 2002 A stochastic projection method for fluid flow. II. Random process. *J. Comput. Phys.* **181**, 9–44.

MASQUELET, M. & MENON, S. 2010 Large eddy simulation of flame-turbulence interactions in a shear coaxial injector. *J. Propul. Power* **26** (5), 925–935.

MASQUELET, M., MENON, S., JIN, Y. & FRIEDRICH, R. 2009 Simulation of unsteady combustion in a LOX-GH_2 fueled rocket engine. *Aerosp. Sci. Technol.* **13** (8), 466–474.

MEECHAM, W. C. & JENG, D. T. 1968 Use of the Wiener–Hermite expansion for nearly normal turbulence. *J. Fluid Mech.* **32**, 225–225.

MENDES, M. A. A., PEREIRA, J. M. C. & PEREIRA, J. C. F. 2011 Calculation of premixed combustion within inert porous media with model parametric uncertainty quantification. *Combust. Flame* **158**, 466–476.

https://doi.org/10.1017/jfm.2014.96 Published online by Cambridge University Press

MITCHELL, C. E., CROCCO, L. & SIRIGNANO, W. A. 1969 Nonlinear longitudinal instability in rocket motors with concentrated combustion. *Combust. Sci. Technol.* **1**, 35–63.

OEFELEIN, J. 2006 Mixing and combustion of cryogenic oxygen–hydrogen shear-coaxial jet flames at supercritical pressure. *Combust. Sci. Technol.* **178** (1–3), 229–252.

OEFELEIN, J. C. & YANG, V. 1993 Comprehensive review of liquid-propellant combustion instabilities in F-1 engines. *J. Propul. Power* **9**, 657–677.

OEFELEIN, J. C. & YANG, V. 1998 Modeling high-pressure mixing and combustion processes in liquid rocket engines. *J. Propul. Power* **14** (5), 843–857.

OTTINO, J. M. 2004 Engineering complex systems. *Nature* **427**, 399–399.

PETRAS, K. 2003 Smolyak cubature of given polynomial degree with few nodes for increasing dimension. *Numer. Math.* **93**, 729–753.

PHENIX, B. D., DINARO, J. L., TATANG, M. A., TESTER, J. W., HOWARD, J. B. & MCRAE, G. J. 1998 Incorporation of parametric uncertainty into complex kinetic mechanisms: application to hydrogen oxidation in supercritical water. *Combust. Flame* **112**, 132–146.

POPE, S. B. 2000 *Turbulent Flows*. Cambridge University Press.

PRIEM, R. J. & HEIDMANN, M. F. 1960 Propellant vaporization as a design criterion for rocket-engine combustion chambers. *NASA Technical Report* R-67. National Aeronautics and Space Administration.

REAGAN, M. T., NAJM, H. N., GHANEM, R. G. & KNIO, O. M. 2003 Uncertainty quantification in reacting-flow simulations through non-intrusive spectral projection. *Combust. Flame* **132**, 545–555.

REARDON, F. H., CROCCO, L. & HARRJE, D. T. 1964 Velocity effects in transverse mode liquid propellant rocket combustion instability. *AIAA J.* **12**, 1631–1641.

SCHMITT, T., MÉRY, Y., BOILEAU, M. & CANDEL, S. 2011 Large-eddy simulation of oxygen/methane flames under transcritical conditions. *Proc. Combust. Inst.* **33**, 1383–1390.

SCHMITT, T., SELLE, L., RUIZ, A. & CUENOT, B. 2010 Large-eddy simulation of supercritical-pressure round jets. *AIAA J.* **48** (9), 2133–2144.

SIRIGNANO, W. A. 1964 Theoretical study of nonlinear combustion instability: longitudinal mode. PhD thesis (Report No. 677), Princeton University Department of Aerospace and Mechanical Sciences, Princeton, NJ.

SIRIGNANO, W. A. 2010 *Fluid Dynamics and Transport of Droplets and Sprays*. 2nd edn. Cambridge University Press.

SIRIGNANO, W. A. & CROCCO, L. 1964 A shock wave model of unstable rocket combustors. *AIAA J.* **2**, 1285–1296.

SIRIGNANO, W. A., DELPLANQUE, J. -P., CHIANG, C. H. & BHATIA, R. 1995 Liquid propellant droplet vaporization: a rate-controlling process for combustion instability. In *Liquid Rocket Engine Combustion Instability* (ed. V. Yang & W. E. Anderson), Progress in Astronautics and Aeronautics, vol. 169, pp. 307–343. American Institute of Aeronautics and Astronautics.

SIRIGNANO, W. A. & POPOV, P. P. 2013 Two-dimensional model for liquid-rocket transverse combustion instability. *AIAA J.* **51**, 2919–2934.

SLUZALEC, A. 2000 Random heat flow with phase change. *Intl J. Heat Mass Transfer* **43**, 2303–2312.

STRAHLE, W. C. 1965*a* Periodic solutions to a convective droplet burning problem: the stagnation point. In *Proceedings of the Tenth Symposium (International) on Combustion*, pp. 1315–1325. The Combustion Institute.

STRAHLE, W. C. 1965*b* Unsteady laminar jet flame at large frequencies of oscillation. *AIAA J.* **3**, 957–960.

STRAHLE, W. C. 1965*c* Unsteady reacting boundary layer on a vaporizing flat plate. *AIAA J.* **3**, 1195–1198.

STRAHLE, W. C. 1967 High frequency behavior of laminar jet flame subjected to transverse sound waves. In *Proceedings of the Eleventh Symposium (International) on Combustion*, pp. 747–754. The Combustion Institute.

TONG, A. & SIRIGNANO, W. A. 1989 Oscillatory vaporization of fuel droplets in unstable combustor. *J. Propul. Power* **5**, 257–261.

TSIEN, H. S. 1952 The transfer function of rocket nozzles. *ARS J.* **22**, 139–143.

https://doi.org/10.1017/jfm.2014.96 Published online by Cambridge University Press

TUCKER, P. K., MENON, S., MERKLE, C. L., OEFELEIN, J. C. & YANG, V. 2007 An approach to improved credibility of CFD simulations for rocket injector design. In *43rd AIAA/ASME/SAE/ASEE Joint Propulsion Conference and Exhibit, Cincinnati, OH*, paper AIAA 2007-5572. American Institute of Aeronautics and Astronautics.

TUCKER, P. K., MENON, S., MERKLE, C. L., OEFELEIN, J. C. & YANG, V. 2008 Validation of high-fidelity CFD simulations for rocket injector design. In *44th AIAA/ASME/SAE/ASEE Joint Propulsion Conference and Exhibit, Hartford, CT*, paper AIAA 2008-5226. American Institute of Aeronautics and Astronautics.

WIENER, N. 1938 The homogeneous chaos. *Am. J. Maths* **60**, 897–936.

WITTEVEEN, J. A. S., LOEVEN, A., SARKAR, S. & BIJL, H. 2008 Probabilistic collocation for period-1 limit cycle oscillations. *J. Sound Vib.* **311**, 421–439.

WITTEVEEN, J. A. S., SARKAR, S. & BIJL, H. 2007 Modeling physical uncertainties in dynamic stall induced fluid–structure interaction of turbine blades using arbitrary polynomial chaos. *Comput. Struct.* **85**, 866–878.

XIU, D. 2010 *Numerical Methods for Stochastic Computations: A Spectral Method Approach*. Princeton University Press.

XIU, D. & KARNIADAKIS, G. 2002 The Wiener–Askey polynomial chaos for stochastic differential equations. *SIAM J. Sci. Comput.* **24** (2), 619–644.

XIU, D. & KARNIADAKIS, G. E. 2003 Modeling uncertainty in flow simulations via generalized polynomial chaos. *J. Comput. Phys.* **187**, 137–167.

XIU, D., LUCOR, D., SU, C. H. & KARNIADAKIS, G. E. 2002 Stochastic modeling of flow structure interactions using generalized polynomial chaos. *J. Fluids Engng* **124**, 51–59.

YANG, B., CUOCO, F. & OSCHWALD, M. 2007 Atomization and flames in LOX/H_2 and LOX/CH_4-spray combustion. *J. Propul. Power* **23**, 763–771.

YANG, V., KIM, S. I. & CULICK, F. E. C. 1990 Triggering of longitudinal pressure oscillations combustion chambers. I: nonlinear gasdynamics. *Combust. Sci. Technol.* **72**, 183–214.

YANG, V. & LIN, N. N. 1994 Vaporization of liquid oxygen (LOX) droplets at supercritical conditions. *Combust. Sci. Technol.* **97**, 247–270.

ZINN, B. T. 1968 A theoretical study of nonlinear combustion instability in liquid-propellant rocket engines. *AIAA J.* **6**, 1966–1972.

ZINN, B. T. & POWELL, E. A. 1971 Nonlinear combustion instability in liquid-propellant rocket engines. In *Proceedings of the Thirteenth Symposium (International) on Combustion*, pp. 491–503. The Combustion Institute.

https://doi.org/10.1017/jfm.2014.96 Published online by Cambridge University Press